Structure of the marine atmospheric boundary layer over an oceanic thermal front: SEMAPHORE experiment

B. Kwon, B. Bénech, Dominique Lambert, P. Durand, A. Druilhet, Hervé Giordani, Serge Planton

JOURNAL OF GEOPHYSICAL RESEARCH, VOL. 103, NO. C11, PAGES 25,159–25,180, OCTOBER 15, 1998

Structure of the marine atmospheric boundary layer over an oceanic thermal front: SEMAPHORE experiment

B. H. Kwon,[1] B. Bénech, D. Lambert, P. Durand, and A. Druilhet
Laboratoire d'Aérologie, Centre de Recherches Atmosphériques, Lannemezan, France

H. Giordani and S. Planton
Centre National de Recherche Météorologique, Météo-France, Toulouse, France

Abstract. The Structure des Echanges Mer-Atmosphere, Proprietes des Heterogeneites Oceaniques: Recherche Experimentale (SEMAPHORE) experiment, the third phase of which took place between October 4 and November 17, 1993, was conducted over the oceanic Azores Current located in the Azores basin and mainly marked at the surface by a thermal front due to the gradient of the sea surface temperature (SST) of about 1° to 2°C per 100 km. The evolution of the marine atmospheric boundary layer (MABL) over the SST front was studied with two aircraft and a ship in different meteorological conditions. For each case, the influence of the incoming air direction with respect to the orientation of the oceanic front was taken into account. During the campaign, advanced very high resolution radiometer pictures did not show any relation between the SST field and the cloud cover. The MABL was systematically thicker on the warm side than on the cold side. The mean MABL structure described from aircraft data collected in a vertical plane crossing the oceanic front was characterized by (1) an atmospheric horizontal gradient of 1° to 2°C per 100 km in the whole depth of the mixed layer and (2) an increase of the wind intensity from the cold to the warm side when the synoptic wind blew from the cold side. The surface sensible heat (latent heat) flux always increased from the cold to the warm sector owing to the increase of the wind and of the temperature (specific humidity) difference between the surface and the air. Turbulence increased from the cold to the warm side in conjunction with the MABL thickening, but the normalized profiles presented the same structure, regardless of the position over the SST front. In agreement with the Action de Recherche Programme te Petite Echelle and Grande Echelle model, the mean temperature and momentum budgets were highly influenced by the horizontal temperature gradient. In particular, the strong ageostrophic influence in the MABL above the SST front seems linked with the secondary circulation due to the SST front.

1. Introduction

Interactions between ocean and atmosphere have been experimentally studied for many years, at scales ranging from the microscale (turbulence) to the synoptic. Many of these experiments focused on the study of physical processes in the marine atmospheric boundary layer (MABL) and of surface turbulent fluxes (e.g., Joint Air-Sea Interactions (JASIN) in 1978 and Humidity Exchange Over the Sea (HEXOS) in 1984). The oceanic mixed layer has also been investigated (e.g., Mixed Layer Experiment (MILE) in 1977). However, the horizontal variability of physical processes in both (atmospheric and oceanic) boundary layers has rarely been experimentally studied; such important variations were revealed for the first time during JASIN, and the Frontal Air-Sea Interaction Experiment (FASINEX), conducted in 1986, was devoted to the study of ocean-atmosphere interactions in inhomogeneous conditions due to the presence of a thermal front in the upper ocean. Many studies with numerical models [*Physick*, 1976; *Rogers et al.*, 1985; *Arrit*, 1993] have been devoted to the evolution of MABL forcing by an ocean front or the analogous sea breeze phenomenon.

The Structure des Echanges Mer-Atmosphère, Propriétés Océaniques: Recherche Expérimentale (SEMAPHORE) experiment was conducted from June to November 1993 south of the Azores islands, in the middle eastern part of the northern Atlantic basin. The experimental area was a 500 km × 500 km box situated between 31°N–38°N and 21°W–28°W. The SEMAPHORE experiment was performed in order to improve knowledge of ocean-atmosphere interactions from the local scale to the mesoscale [*Eymard et al.*, 1996]. SEMAPHORE presents many similarities with FASINEX concerning the behavior of the MABL forced from the surface by a sea surface temperature (SST) front as a function of the incoming flow (from the warm sector or cold sector or nearly parallel to the SST front).

The third phase of the SEMAPHORE experiment was conducted between October 4 and November 17, 1993. During this period, the MABL was investigated by ship and aircraft over the sea surface temperature front. The R/V *Le Suroît* embarked both oceanic and atmospheric sensors. Two aircraft, a Fokker 27 (F27) instrumented by the French Institut National des Sciences de l'Univers and a Fairchild Merlin IV (MIV)

[1] Now at Department of Astronomy and Atmospheric Sciences, Kyungpook National University, Taegu, Korea.

Paper number 98JC02207.
0148-0227/98/98JC-02207$09.00

equipped by the French Meteorological Office, were used to document surface fluxes and MABL characteristics. These measurements were complemented by geophysical parameters derived from drifting buoys and operational meteorological satellites (Meteosat, National Oceanic and Atmospheric Administration (NOAA) and Defense Meteorological Satellite Program). This paper presents the MABL characteristics analyzed mainly from data collected by the two aircraft above the oceanic thermal front. The ship measurements represented the reference for SST and atmospheric surface measurements.

In section 2, experimental designs and data processing are presented. Synoptic and local characteristics of the atmosphere for the different cases are then be described. In section 3 the structure and spatial variability of the surface characteristics, as well as the mean and turbulent structure of the MABL above the SST front, will be analyzed. In section 4 the heat and momentum budget in the MABL are examined. To complement the measurements, selected results from the sequence of analysis of forecast and the forecast runs of the Action de Recherche Programme te Petite Echelle et Grande Echelle (ARPEGE) model of the French national weather service will be used throughout this paper, in particular, to characterize the structure of the SST field and to gain insight into various terms of the heat budget. Simulations with the ARPEGE model of several cases from SEMAPHORE are presented by *Giordani et al.* [this issue]. It is difficult to make quantitative comparisons between the different experiments owing to the fact that the MABL is described with aircraft along a vertical plan crossing the SST front at different angles. To find a common reference for these different experiments, MABL two-dimensionality is assumed and the physically relevant horizontal coordinate is the distance along a line parallel to the SST gradient. (see Figure 4).

2. Experimental Design

2.1. Instrumentation and Data Processing

2.1.1. Instrumented aircraft. Both aircraft had the same capabilities for measuring turbulence and radiation, although the sensors were different. The F27 was equipped with a 5-m-long nose boom, on the tip of which were installed fast response sensors. They consisted of a Rosemount 858 probe, which measured static and dynamic pressure and attack and slide-slip angles. An inertial navigation system (INS), installed close to the gravity center of the aircraft, measured the aircraft horizontal geographical position, the ground velocity vector, and the attitude angles of the aircraft (pitch, roll, and true heading). On the MIV, total pressure as well as attack and slide-slip angles were measured on a "radome" installed on the aircraft nose, following the principle described by *Brown et al.* [1983]. The INS (same as in the F27) was installed just behind the nose of the aircraft. On both aircraft, temperature was measured by a Rosemount 102E2-AL probe and moisture was measured by a dew-point hygrometer and a Lyman-α sensor. Radiation measurement involved upward and downward looking longwave (2π sr, 4- to 40-μm band Eppley sensors) and shortwave radiometers (2π sr, 0.2- to 2.8-μm band Eppley) and a downward looking Barnes PRT5 thermoradiometer for sea surface brightness temperature measurements. The altitude above the surface was measured by a radioaltimeter. The sampling rate (maximum of 256 s^{-1} on the F27 and 50 s^{-1} on the MIV) varied according to the time response of the sensors.

Turbulence processing concerned the three wind components (u', v', and w'), the potential temperature θ', and specific humidity q'. Turbulence samples were then defined as straight and level runs of roughly 5 min (about 27 km). The fluctuations were calculated in the frame of reference defined by the horizontal mean wind and the vertical coordinate. The instantaneous wind vector was calculated, using a standard algorithm, from the measurement of dynamic pressure, attack and side-slip angles, and the ground velocity provided by the INS (see, for instance, *Lenschow* [1986]). Static temperature was deduced from the impact temperature measurement, after correction of the adiabatic heating due to aircraft airspeed. The specific humidity was calculated from the Lyman-α signal, after calibration against the dew-point hygrometer.

Turbulent fluxes were calculated by the eddy correlation technique. After detrending the signals along each run, a high-pass filter was applied, with a cutoff corresponding approximately to a wavelength of 5 km, which resulted in a satisfactory compromise for minimizing the total error on the flux computation [*Lambert and Durand*, this issue]. For data processing, the raw parameters were reduced to a sampling rate of 16 s^{-1} for the F27 and 25 s^{-1} for the MIV, which corresponded to a resolution of about 4 to 5 m. The intercomparison of the two aircraft made during the SEMAPHORE experiment was analyzed by *Lambert and Durand* [this issue], who showed good agreement for the mean and turbulent parameters. A bias of 0.7°C between the temperature sensors of the two aircraft was detected. The Merlin was taken as reference, and the Avion de Recherches Atmosphériques et de Télédetection (ARAT) measurements were corrected when the two aircraft were simultaneously used for the analysis of the MABL structure.

The SST was estimated from the Barnes radiometer located on the aircraft, after correction of the vertical divergence of the radiation between the surface and the flight level, estimated to average 2.5×10^{-3} K m^{-1}. A rough estimation of the error due to the incoming longwave radiation, whose influence can be considerable as long as the surface emissivity significantly differs from 1, was evaluated to be 0.5°C.

2.1.2. Shipborne measurements. Aboard the *Le Suroît*, most operations were performed with simultaneous measurements in the ocean and the atmosphere. Atmospheric measurements involved four radiosonde soundings per day and mean meteorological measurements in the atmospheric surface layer including temperature, moisture, wind, and radiation (net radiation and incoming shortwave and longwave radiation). Turbulence measurements were performed on a mast located on the foredeck of the ship by a sonic anemometer and a Lyman-α sensor, from which the sensible heat, latent heat, and momentum fluxes were deduced via the inertial dissipation method [see *Dupuis et al.*, 1997]. From these fluxes and the mean meteorological measurements, *Dupuis et al.* [1997] computed the drag coefficient and the bulk coefficients for sensible heat and latent heat fluxes. The sea temperature was measured at a depth of 2.5 m, and in the following sections it is considered to be similar to the sea surface temperature.

2.1.3. Surface flux measurements. The surface fluxes of sensible heat, latent heat, and momentum were computed from data from both the instrumented ship and the aircraft. *Durand et al.* [this issue] performed an intercomparison between these two platforms. Taking into account that the lowest flight level (generally 90 m) was above the "constant flux" surface layer, surface values had to be deduced from an extrapolation toward the surface of the flux profiles computed from vertically stacked runs. *Durand et al.* [this issue] showed

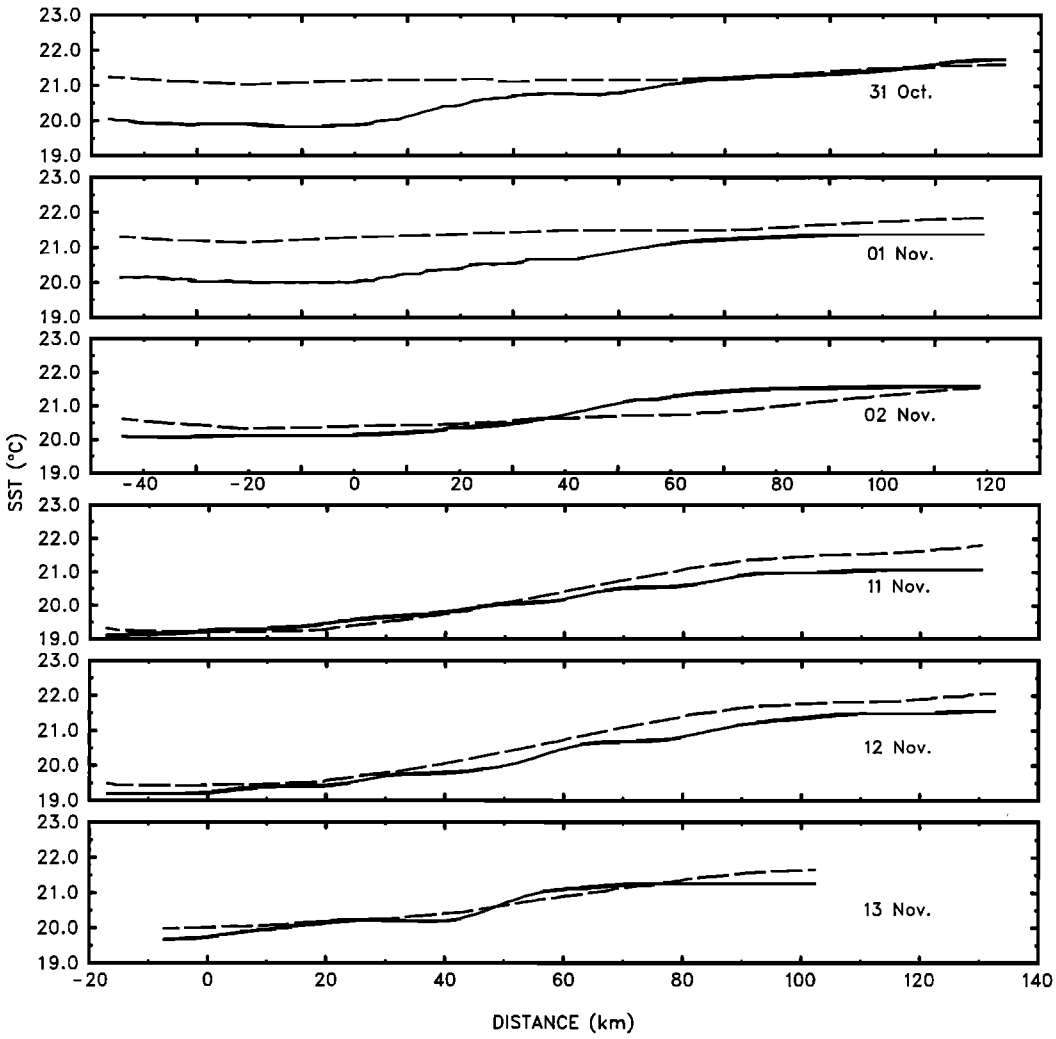

Figure 1. Sea surface temperature (SST) along the aircraft track as denoted from aircraft measurement (solid curves) and from the Action de Recherche Programme Petite Echelle et Grande Echelle (ARPEGE) analysis at 1200 UT (dashed curves).

that the momentum flux agreed fairly well, but aircraft estimations of sensible and latent heat flux were consistently lower than those from the ship. The underestimation was greater for sensible heat flux (37%) than for the latent heat one (13%).

2.1.4. SST field. The SST measurements made by the ship were, on average, 1°C greater than those performed by the Merlin IV. This is not surprising, because the two measurements systems were very different; the aircraft measured the brightness of the surface (including air-sea mixing), whereas the ship measured the temperature 2.5 m under the surface. We considered the ship measurements as a reference and accordingly corrected the aircraft measurements. SST measurements made by ship and buoys were assimilated in the ARPEGE model analysis [*Giordani et al.*, this issue]. This work provided, for the whole experiment, SST maps on which the location of the temperature front could be easily determined. The orientation of the aircraft patterns with respect to the SST isolevels could therefore be precisely known. On the other hand, when we analyze the MABL structure over the SST front along the flight axis, we consider the SST measurements performed by the aircraft along its track. Figure 1 presents, for six experiments during SEMAPHORE, the comparison of the SST deduced from aircraft data with that deduced from the ARPEGE analysis along the flight axis and projected along the reference axis. In general, a very good agreement was found, except for the October 31 and November 1 cases. This large departure was due to the time lag of the ARPEGE analysis to assimilate the rapid SST change in response to the storm of October 29 in the northern part of the domain [see *Giordani et al.*, this issue]. Nevertheless, the ARPEGE analysis can be used in most of the situations to locate the flight track with respect to the SST front orientation. The SST maximum gradient between the cold and the warm sector, deduced from the ARPEGE analysis and from experimental data, was about 1° to 2°C per 100 km (Figure 1).

2.2. Experimental Procedure

During each intensive observation period (IOP) the ship and the two aircraft simultaneously operated in the same area. For the 10 IOPs, flight plans varied according to wind and SST front orientation. Generally, the aircraft performed horizontal runs 250 to 300 km long, oriented along the SST gradient, at

several altitudes (three to six) in the MABL. In some cases, three perpendicular branches, situated at each end and in the middle of this main axis, were also run at several altitudes. The lowest run was generally at a 90-m altitude, and the highest was at the MABL top or cloud base. At each extremity and in the middle of the principal axis, the aircraft performed a vertical sounding from the lowest altitude up to well above the capping inversion that marks the top of the boundary layer. These flights lasted 3 to 4 hours, during which it is assumed that meteorological conditions did not vary too much. Flight tracks and ship position are indicated in Figure 3 for the six cases analyzed in this paper.

3. Case Analysis

Two periods were analyzed. The first (October 31 and November 1 and 2 1993) was characterized by low atmospheric pressure associated with an atmospheric front crossing the experimental area during which the MABL was influenced by synoptic effects. The second (November 11–13, 1993) presented high-pressure situations during which the MABL structure was controlled by local effects.

3.1. Mean Meteorological Conditions

The SEMAPHORE domain was characterized by the semipermanent anticyclone known as the "Azores High." Figure 2 gives surface meteorological charts for the two characteristic periods and the position of the experimental area. During the first period the SEMAPHORE domain was affected by active low-pressure systems that generated cold advection. On October 31 an active low-pressure (1000 hPa) center, located near 35°N–17°W at 1200 UT, slowly moved toward the northeast. The northern part of the domain was influenced by a quasi-stationary, not very active front. The northerly wind decreased from about 20 to 15 knots (10 to 7.5 m s^{-1}) at 1200 UTC in the afternoon. On November 1 the domain was influenced by both a low-pressure system (1000 hPa) located southeast of Portugal and another one located in the northern Atlantic. On the SEMAPHORE domain the pressure field increased up to 1018 hPa in the evening. The northwest wind decreased during the day from 10 to a few knots (5 to a few meters per second) at 1200 UTC. On November 2 the high pressure decreased under the influence of the active, low-pressure system located on the northern Atlantic. The wind, which blew from the west (between 15 and 30 knots (7.5 and 15 m s^{-1}) at 1200 UTC) in the morning, turned to become north-northwest in the afternoon when the cold front crossed the domain.

During the second period, the anticyclone (1037 hPa) centered north of the Azores slowly moved eastward on November 11. The cold front located to the east of the SEMAPHORE domain progressively disappeared. The wind was northeasterly (10 to 15 knots (5 to 7.5 m s^{-1}) at 1200 UTC). On November 12 the stationary anticyclone was centered on the SEMAPHORE domain and the wind (5 knots (5 m s^{-1}) was northeasterly oriented but locally weak and variable. On November 13 the anticyclone slowly moved toward the east and the wind was more easterly than on November 12.

3.2. SST Field and Cloud Cover

For each analyzed day, Figure 3 presents, in the SEMAPHORE domain, (1) the SST field derived from the ARPEGE analysis, (2) the albedo (in percent) deduced from visible advanced very high resolution radiometer (AVHRR) data (0.58–0.68 μm), and (3) aircraft tracks (segments labeled AB) and ship position (denoted "s"). The SST field is characterized by a large meander, oriented NW–SE in the northwestern area of the SEMAPHORE domain and W–E in the southern area. All the aircraft flights took place in the northwestern part of the meander where the SST gradient was increased between a thermal dipole whose minimum (19.2°C) was located at 24.8°W–36°N and maximum (23.4°C) was located at 27.5°W–34.8°N. The SST front was quasi-stationary during the whole campaign, although local deformations were observed in the minimum temperature area. In the flight zone the SST front orientation (with respect to north) changed from 20° on October 31 to 30° on November 13. The mean gradient of 1° to 2°C per 100 km was maintained throughout the duration of the experiment. These values were much lower than those observed during the FASINEX experiment [*Rogers*, 1989; *Friehe et al.*, 1991]. Table 1 gives the principal characteristics of the flights discussed herein.

The cloud cover can be analyzed from the visible radiation measured by the AVHRR sensor on NOAA satellites. We assume that a pixel is cloudy when the albedo is greater than 10%. On October 31 at 1656 UT, the cloud cover was more dense in the western part of the domain near the flight area than in the eastern part (Figure 3a). During the aircraft flights (1308–1632 UT) a stratocumulus (Sc) layer was observed, rather solid near point A (36°67′N, 26°17′W) and rather broken near point B (35°00′N, 26°16′W). Showers were locally observed. Ship position (s) (35°00′N, 26°16′W) was near B. On November 1 the albedo at 0849 UT was low in the flight zone but high in the southeastern part of the domain (Figure 3b). Cloud cover observed along the flight path (same as for the previous day) between 1321 and 1624 UT consisted of thin Sc near A and cumuli (Cu) near B without precipitation. On November 2, cloud cover at 1631 UT was very dense (high albedo) over the whole domain but decreased from north to south (Figure 3c). The Sc layer, capping the MABL, was solid in A and broken in B at the beginning of the aircraft flights (1144 UT). At the end of the flights (1523 UT), cloud cover was denser and uniform and preceded a cold front. During this first period (October 31 to November 2), cloud cover was therefore controlled by the synoptic meteorological condition rather than by the SST field.

We now consider the anticyclonic period. Cloud cover was very low on November 11 over the flight area (albedo <5% at 0833 UT) (Figure 3d). Along the flight track, flown between 1145 and 1523 UT, some Cu were observed near A (36°76′N, 24°63′W), whereas clear sky was observed in B (34°64′N, 26°22′W). On November 12, only the northern part of the SEMAPHORE domain can be observed on the AVHRR picture at 0953 UT. This picture revealed an increase of cloud cover toward the east (Figure 3e). The same phenomenon can be observed on the image of November 13 at 0931 UT (Figure 3f). On November 12, in the flight area, the Cu layer was very sparse between A (36°74′N, 24°64′W) and B (34°64′N, 26°22′W), which was also the case for November 13 between A (36°45′N, 26°00′W) and B (34°85′N, 26°17′W). On November 13, in the flight area, a cloud mesoscale structure can be observed near A. During the JASIN experiment, low-level cloud structure changes were observed in response to the SST change [*Guymer et al.*, 1983]. During FASINEX, *Rogers* [1989] reported that an organization of low cloud cover was related to the SST field on day 48. In the SEMAPHORE experiment, analysis of two AVHRR pictures per day with different chan-

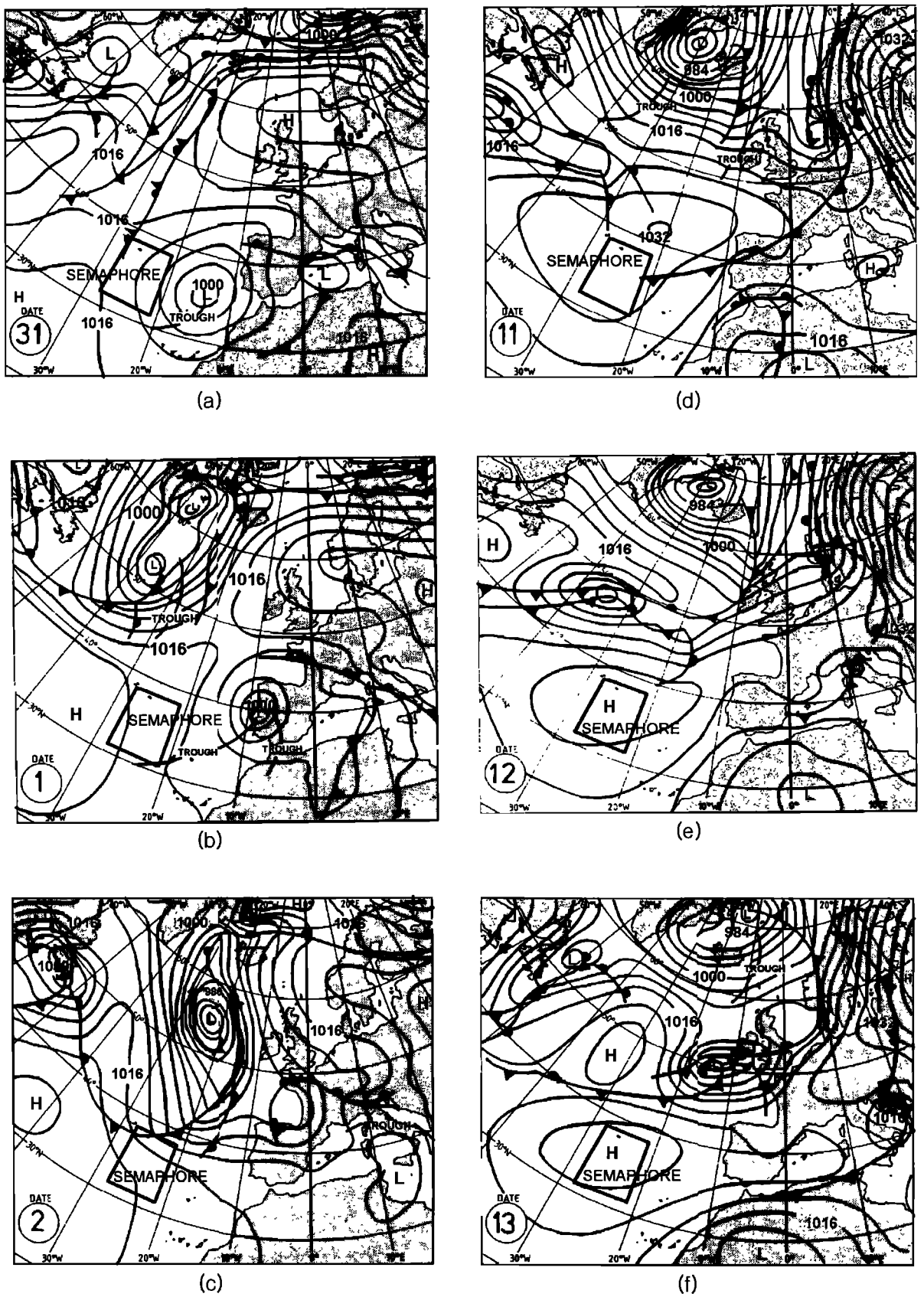

Figure 2. Surface pressure charts at 1200 UT for the low-pressure period, (a) October 31, (b) November 1, and (c) November 2, and the high-pressure period, November (d) 11, (e) 12, and (f) 13. Structure des Echanges Mer-Atmosphere, Proprietes de Heterogeneites Oceaniques: Recherche Experimentale (SEMAPHORE) domain is indicated (shaded area).

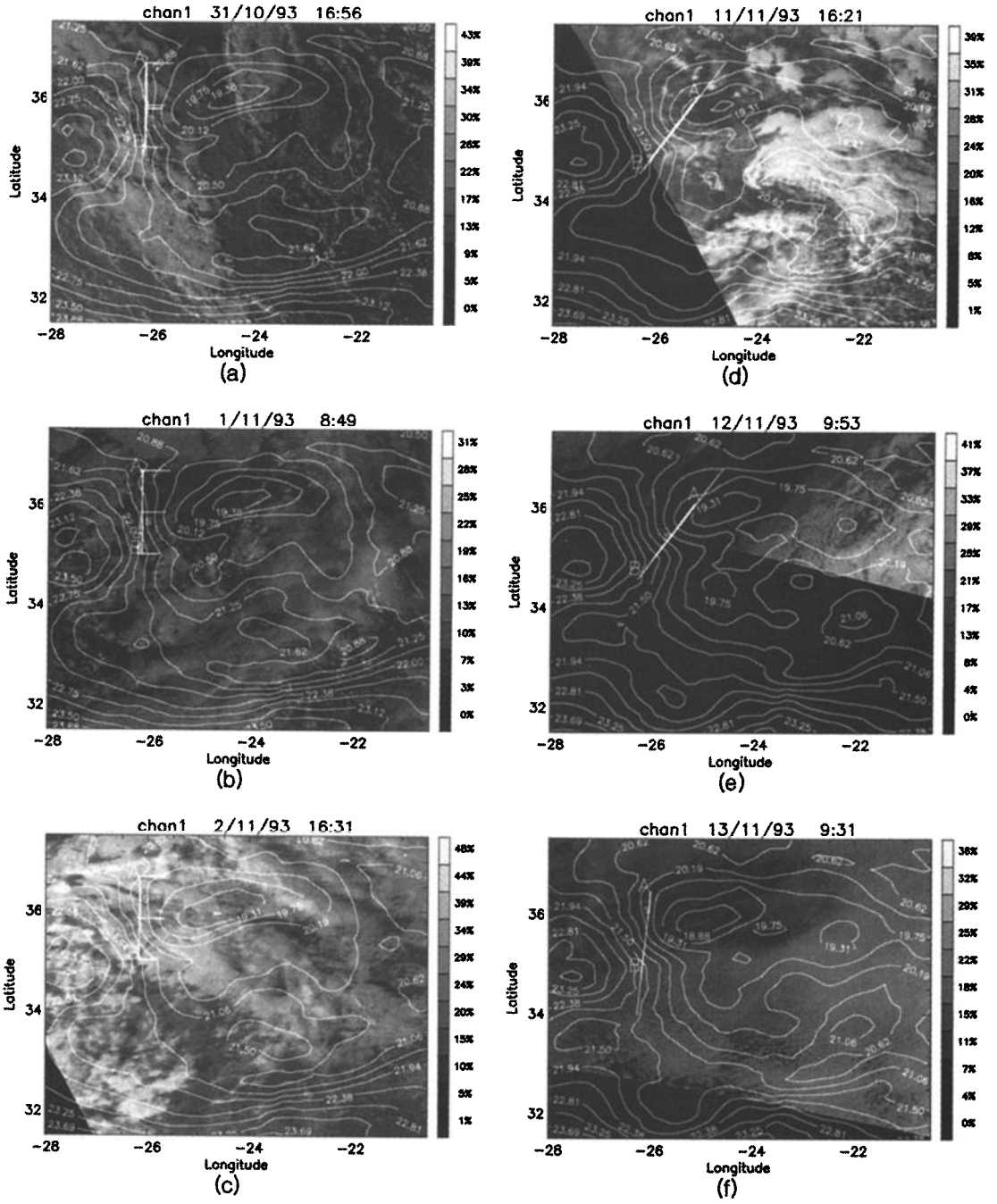

Figure 3. SST field at 1200 UT deduced from ARPEGE (isolines) superimposed on advanced very high resolution radiometer (AVHRR) images (visible channel) on the SEMAPHORE domain on (a) October 31 and November (b) 1, (c) 2, (d) 11, (e) 12, and (f) 13, 1993. Times of the satellite overpass are indicated at top. Flight tracks (straight lines), ship positions during flights (denoted by "s"), and reference points (A and B) are also indicated.

nels did not reveal any particular cloud organization related to the SST field, even during anticyclonic periods when the local effects can be more efficient with respect to the synoptic meteorological conditions.

3.3. Atmospheric Flow Versus SST Front

Table 2 and Figure 4 give, for each experiment, mean direction of the MABL wind and orientations of the SST front and the main flight axis. In the low-pressure period we observed three different orientations of the atmospheric flow with respect to the SST front: (1) the wind blew from the cold sector and the flight axis was nearly parallel to the wind (October 31), (2) the atmospheric flow was quasi-parallel to the surface isotherms and the flight axis was nearly parallel to the wind (November 1), and (3) the wind blew from the warm to the cold water and the flight axis was perpendicular to the atmospheric flow (November 2). In the anticyclonic period (November 11–13) the wind systematically blew from the cold to

Table 1. Flight Times and Geographical Positions of the Extreme Limit A and B of the Flight Axis and the Ship Position(s) During Flight Time

Date, 1993	Flight Time, UT	Aircraft Position		Ship Position(s) During Flight
		A	B	
Oct. 31	1308–1632	26°17'W, 36°76'N	26°16'W, 35°00'N	26°17'W, 34°85'N
Nov. 1	1321–1624	26°18'W, 36°65'N	26°15'W, 35°00'N	26°05'W, 35°60'N
Nov. 2	1144–1505	26°16'W, 36°64'N	26°15'W, 35°02'N	26°00'W, 36°15'N
Nov. 11	1145–1523	24°63'W, 36°76'N	26°22'W, 34°64'N	26°10'W, 34°75'N
Nov. 12	1241–1537	24°64'W, 36°76'N	26°21'W, 34°66'N	25°72'W, 35°35'N
Nov. 13	1051–1307	26°00'W, 36°45'N	26°17'W, 34°85'N	26°04'W, 36°02'N

the warm water. On November 11 the flight axis was oriented along the wind direction, whereas it made an angle of 45° on November 12 and was nearly perpendicular on November 13.

4. Mean Structure of the MABL Above the SST Front

4.1. MABL Thickness and Global Characteristics

Although the flights took place in different zones over the SST front, MABL characteristics were always different in the cold and warm zones. Figure 5 and Table 3 present, for each experiment, the MABL structure in A (colder zone) and B (warmer zone) defined in Table 1 and Figure 3.

The MABL was composed of a well-mixed layer extending from the surface to altitude h, topped by a slightly stable layer itself topped by the Sc layer whose summit (altitude Z_t) presented a strong temperature inversion and an important drying. The strength of this inversion was greater in the anticyclonic period than in the low-pressure period (Figure 5). The MABL thickness Z_i, which corresponded to the altitude of the cloud top, was higher on the warm side than on the cold side, except for November 11. The inversion was generally very strong (5°C/200 m) and its altitude varied considerably between the two periods (Table 3 and Figure 5). The mixed layer thickness h, deduced from the profiles of turbulence characteristics [*Lambert and Durand*, this issue], was always significantly lower than Z_i. Therefore the stratocumulus layer was generally decoupled from the turbulence that originated from the sea surface [*Lambert*, 1997], as shown by *Réchou et al.* [1995] from the Surface de l'Octan, Flux et Interaction avec l'Atmosphere (SOFIA) experiment (which was performed in the same area as SEMAPHORE). The h was always higher in the warm sector than in the cold sector, and the mean temperature (at a given altitude) was always colder in A than in B, unlike the specific humidity, which was too variable to identify a systematic variation between the cold and the warm side.

Table 3 presents mean parameters estimated at the conventional altitude of 10 m, computed from aircraft data. Temperature T_{10} was extrapolated from the lowest flight level according to the constant potential temperature law, whereas the specific humidity q_{10}, the wind velocity U_{10}, and the wind direction D_{10} were assumed to be identical to those measured by the aircraft at the lowest flight level (generally 90 m). In other words, it was assumed that the vertical gradients were low between 10 m and the top of the surface layer. This hypothesis was verified for the wind profile, for which the application of a power law proposed by *Panofsky and Dutton* [1984], between 90 and 10 m, with a value of the exponent p equal to 0.1 in neutral condition and 0.06 in unstable condition, did not give a reduction of wind intensity greater than 0.5 m s^{-1}. Furthermore, comparisons with the ship measurements showed a good agreement with this hypothesis [*Durand et al.*, this issue].

The surface fluxes were deduced by extrapolation toward the surface of flux profiles computed from the four flight runs vertically stacked between 90 m and the top of the mixed layer. Friction velocity u_* was defined as the square root of the total momentum flux per unit mass at the surface. The values of u_* increased from the cold side to the warm side, except for November 2 and 13, where u_* was nearly constant. This increase was in agreement with the wind increase. Surface sensible heat flux Q_H was lower than 21 W m^{-2} and systematically increased from the cold to the warm sector. Surface latent heat flux Q_L, of the order of 100 W m^{-2}, also increased from the cold side to the warm side. The Monin-Obhukov length L was calculated from the friction velocity and the surface buoyancy flux, the latter involving the contribution of the temperature and moisture fluctuations. L, as well as the ratio $-h/L$, which is a global stability index for the mixed layer, did not significantly vary between the cold and the warm sector. Values of

Table 2. Wind, Sea Surface Temperature Front, and Flight Axis Direction

Date, 1993	Direction			Comments
	MABL Wind, °N	SST Front, °N	Flight Axis, °N	
Oct. 31	340–360	340	0	wind blows parallel to SST front and flight axis
Nov. 01	330–340	340	0	wind blows parallel to SST front and flight axis
Nov. 02	260–280	335	0	wind blows from warm sector to cold sector
Nov. 11	10–40	335	30	wind blows from cold sector to warm sector
Nov. 12	70–80	330	30	wind blows from cold sector to warm sector
Nov. 13	100–120	330	10	wind blows from cold sector to warm sector

MABL is marine atmosphere boundary layer.

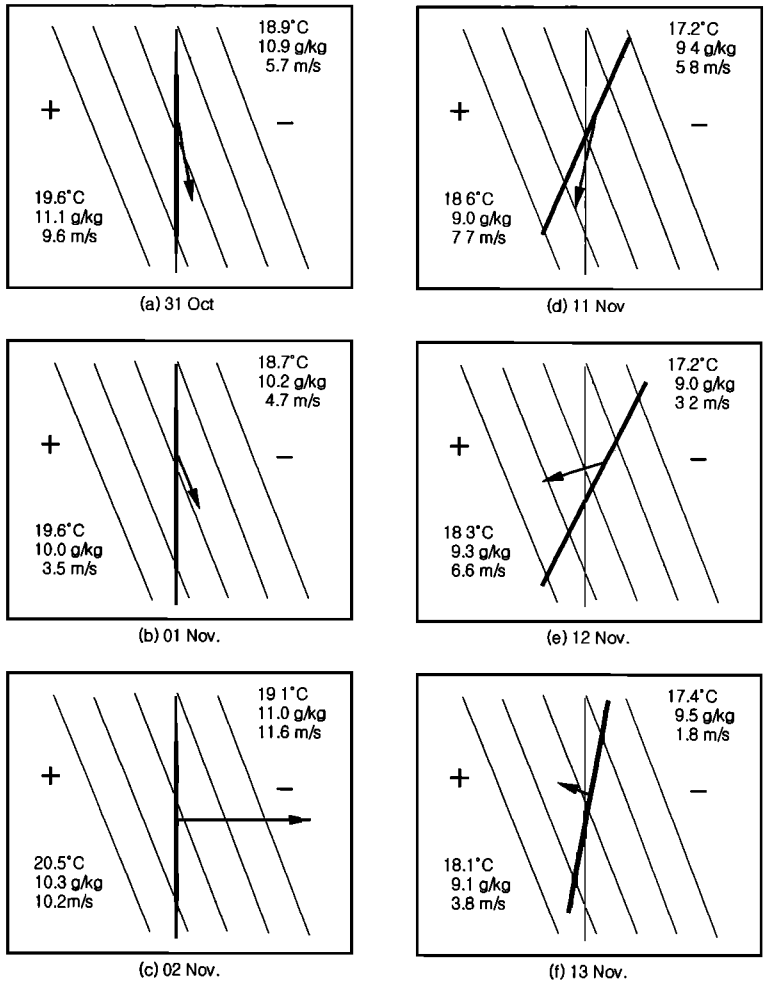

Figure 4. Diagrammatic representation of wind flows (arrows) versus SST field (thin lines) and aircraft tracks (thick lines) on (a) October 31 and November (b) 1, (c) 2, (d) 11, (e) 12, and (f) 13. SST, mixing ratio, and wind velocity corresponding to Table 2 are given in the warm side (pluses) and cold side (minuses). Dotted line is the axis parallel to the SST gradient used as a reference axis in the figures describing the MABL evolution above the thermal front.

$-h/L$, ranging between 2 and 80, were far from free convection conditions. Surface layer scales were defined from surface fluxes ($T_* = -\overline{w'\theta'}/u_*$ and $Q_* = -\overline{w'q'}/u_*$), whereas the convective scales θ_* and w_* were defined for the whole mixed layer according to *Deardorff* [1970]. The convective moisture scale was defined as $Q_{**} = \overline{w'q'}/w_*$.

4.2. Mean Thermodynamical Structure of the MABL

The aircraft data mean temperature and humidity (averaged over 1 km along the aircraft track) were interpolated between the different flight levels in order to describe the principal features of the mixed layer structure in the vertical plane projected along the axis parallel to the SST gradient. The low-pressure (October 31 and November 1 and 2) and high-pressure cases (November 11–13) are presented in Figures 6a and 6b, respectively. In the image for each day the potential temperature field, superimposed by the wind vector, and the SST variation are presented at left, whereas the specific humidity field superimposed by the wind vector and the surface buoyancy flux are shown at right. The air potential temperature increased, as did the SST, in the whole depth of the mixed layer. This relationship did not depend on the incoming airflow direction and was valid for the two periods, although it was more pronounced in the high-pressure period than in the low-pressure one. The humidity fields were more variable, and no clear tendency can be generalized.

The horizontal gradient of air temperature was generally smaller than the SST gradient and sometimes decreased with height. These features were due to both the thermal advection linked with the synoptic flow and the local sensible heat flux. As a result, the location of the horizontal gradients of temperature or humidity was not systematically correlated with the position of the SST gradient as shown in Figures 6a and 6b on October 31 and November 1 and 13. The same behavior is shown also with the ARPEGE model by *Giordani et al.* [this issue].

4.3. MABL Wind Structure

Except for the cases of November 1 and 2, where the wind was linked to the synoptic situation, in all other cases where the wind blows from the cold to the warm side, the wind field was characterized by (1) an increase of the wind intensity from the cold to the warm sector and (2) a small decrease of the wind intensity with altitude, especially in the warm sector where the

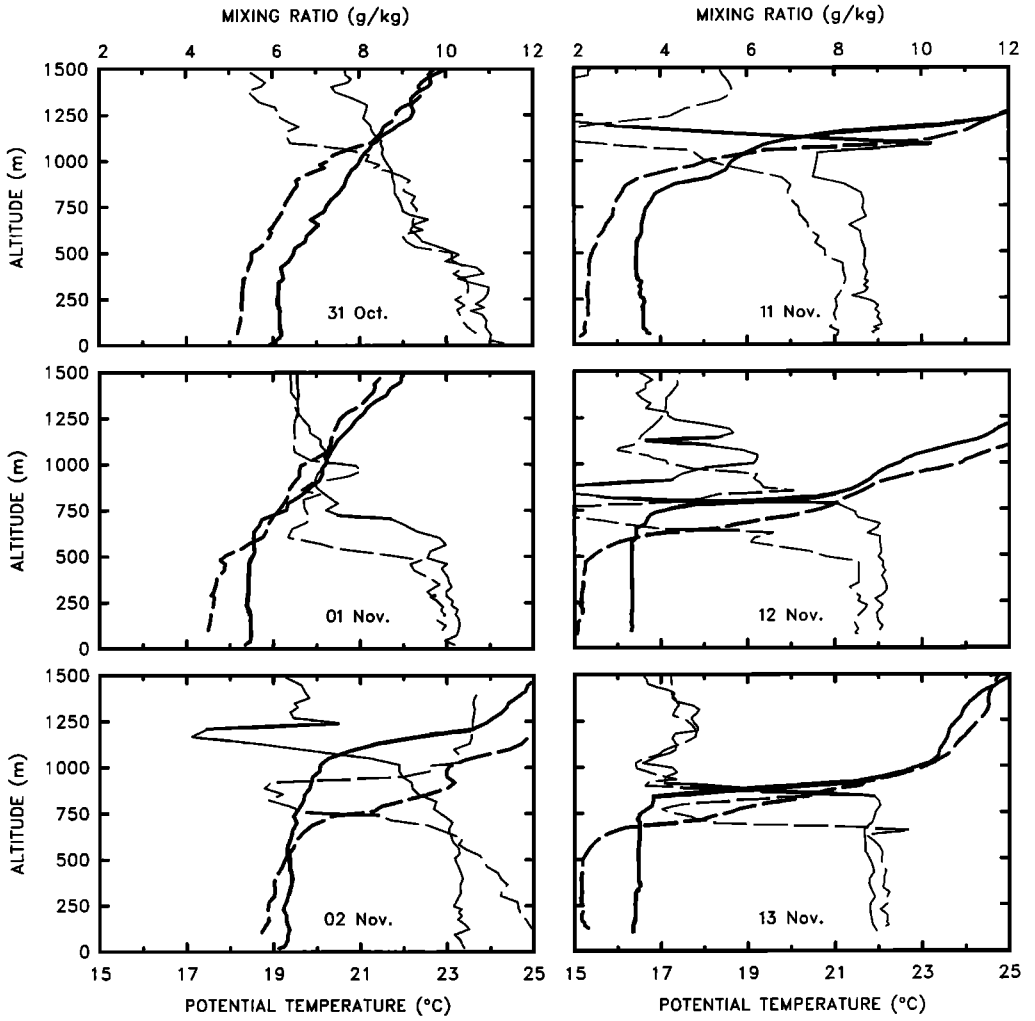

Figure 5. Profiles of potential temperature (thick solid curves) and humidity mixing ratio (thin solid curves) on the cold (thick dashed curves) and warm (thin solid curves) sides of the SST front. Dates are indicated on each graph.

wind was maximum at low level and during the anticyclonic period (Figure 7).

5. Variation of the Surface Flux Across the SST Front

Figure 8 shows a good correlation, independent from the air mass origin, between the horizontal variation of the surface fluxes Q_H and Q_L and that of the SST across the oceanic thermal front for the two analyzed periods. The increase of Q_H and Q_L was more important during high-pressure periods (13 to 16 W m^{-2} for Q_H and 39 to 113 W m^{-2} for Q_L) than during low-pressure ones (6 to 11 and 7 to 72 W m^{-2}, respectively). During FASINEX, *Friehe et al.* [1991] showed that the increase of the turbulent heat fluxes is linked with the orientation of the incoming flow. They found, as during SEMAPHORE, that the increase of the heat fluxes is high when the incoming flow comes from the cold sector (FASINEX case of February 16, 1986). This is due to the fact that the cold air advected above the SST front maintains its thermodynamical properties above the SST front. When the wind is parallel to the SST front, the increase of the heat fluxes is small, as seen during FASINEX (case of February 17, 1986). When the air flow comes from the warm sector, the sensible heat flux during SEMAPHORE remains weakly positive in the cold sector. During FASINEX (case of February 18, 1986), *Friehe et al.* [1991] report that the sensible heat flux is negative above the cold sector, owing to the stability brought by the advection of the warm air above the cold water and the presence of an internal boundary layer. This phenomenon was not observed during SEMAPHORE from the aircraft analysis.

The friction velocity u_* was generally weak, and its intensity was well correlated with the wind speed (see Table 3). In particular, during the high period, u_* increased from the cold to the warm sector according to the increase of the wind.

The observed increases of Q_H and Q_L across the SST front were due to both the increase of the flow intensity and the increase in the difference of temperature and humidity between the air and the sea surface. The respective contributions of these two terms to Q_H and Q_L can be computed with the bulk formulas

$$Q_H = \rho C_p C_H U_{10}(\mathrm{SST} - T_{10}) \quad (1)$$

$$Q_L = \rho L_w C_Q U_{10}(q_s - q_{10}) \quad (2)$$

Table 3. Boundary Layer Parameters

	Oct. 31 (1)		Nov. 1 (2)		Nov. 2 (3)		Nov. 11 (4)		Nov. 12 (5)		Nov. 13 (6)	
	A	B	A	B	A	B	A	B	A	B	A	B
Cloudiness	6/8	7/8	8/8	4/8	8/8	4/8	3/8	0/8	0/8	4/8	6/8	6/8
SST, °C	20.1	21.7	20.2	21.4	20.3	21.6	19.2	21.0	19.2	21.5	19.8	21.3
T_{10}, °C	18.9	19.6	18.7	19.6	19.1	20.5	17.2	18.6	17.2	18.3	17.4	18.1
q_{10}, g kg^{-1}	10.9	11.1	10.2	10.0	11.0	10.3	9.4	9.0	9.0	9.3	9.5	9.1
U_{10}, m s^{-1}	5.7	9.6	4.7	3.5	11.6	10.2	5.8	7.7	3.2	6.6	1.8	3.8
D, deg	11	358	346	340	259	285	41	12	76	72	127	96
Z_i, m	2400	2600	2300	2400	~2000	~2000	1150	900	700	790	750	850
h, m	358	440	485	670	530	700	455	700	520	675	675	755
u, m s^{-1}	0.19	0.26	0.09	0.12	0.29	0.28	0.14	0.22	0.09	0.14	0.22	0.22
Q_{L0}, W m^{-2}	53.2	125.0	66.0	72.8	86.8	148.6	69.6	159.4	42.0	155.1	54.7	93.4
Q_{H0}, W m^{-2}	3.4	14.3	4.2	10.1	4.5	10.3	3.3	16.1	5.3	21.5	6.6	18.3
$-L$, m	80	74	7	11	199	94	30	36	7	8	87	36
$-h/L$	4.8	6.0	68.8	60.0	2.7	7.5	15.1	19.5	77.1	80.5	7.8	20.7
$-T*$, K	0.032	0.068	0.082	0.102	0.031	0.062	0.047	0.101	0.079	0.183	0.039	0.094
$-Q*$, g kg^{-1}	0.098	0.130	0.252	0.200	0.103	0.182	0.165	0.241	0.164	0.360	0.084	0.145
$w*$, m s^{-1}	0.424	0.638	0.491	0.656	0.538	0.738	0.467	0.806	0.489	0.843	0.577	0.802
$\theta*$, K	0.014	0.028	0.015	0.019	0.016	0.023	0.014	0.028	0.014	0.031	0.015	0.025
$Q**$, g kg^{-1}	0.043	0.053	0.045	0.038	0.055	0.069	0.049	0.066	0.028	0.062	0.031	0.039

Numbers in parentheses correspond to Figures 6 and 8. A is the colder zone, while B is the warmer zone. Variables are defined as follows: SST, sea surface temperature, $T_{10}*$, air temperature; $q_{10}*$, air moisture; and U_{10}, wind intensity, all at 10 m above sea level; D, wind direction at 10 m above sea level; Z_i, height of the thermal inversion linked with the marine atmospheric boundary layer; h, height of to atmospheric mixing layer; u^*, friction velocity; Q_{L0}, latent heat flux; Q_{H0}, sensible heat flux; L, Monin Oohukov length; $-h/L$, stability parameter; I^*, surface layer temperature scale; Q^*, surface layer moisture scale; θ_*, convective temperature scale; $Q**$, convective moisture scale.

where ρ is air density; C_p is the specific heat at constant pressure; L_w is the latent heat of vaporization of water; C_H and C_Q are the bulk coefficients for heat and moisture, respectively; U_{10} is the wind speed in the low atmosphere (10 m); and SST $- T_{10}$ $(q_s - q_{10})$ is the difference in temperature (specific humidity) between the surface and the value at 10 m above the sea surface. A drag coefficient C_D can be defined in a similar manner for the momentum transfer ($u_*^2 = C_D U^2$). The coefficients C_D, C_H, and C_Q were calculated using corrections for height and stability as suggested by *Dupuis et al.* [1997]. This parameterization is suitable for low wind speeds as encountered during SEMAPHORE.

A satisfactory agreement was found between the sensible heat and latent heat fluxes measured by aircraft and those deduced from the bulk formulas (Figure 9a). If we assume that the variations of C_H and C_Q along the flight axis are negligible, we can thus evaluate the respective contribution to the flux increase of the wind (mechanical term) and of the variation of SST $- T_{10}$ and $q_s - q_{10}$ ("thermal term" and "humidity term," respectively) by derivation of (1) and (2) with respect to the horizontal distance:

$$\frac{dQ_H}{dx} = \rho C_p C_H \left[\overline{(\mathrm{SST} - T_{10})} \frac{d\bar{U}}{dx} + \bar{U} \frac{d\overline{(\mathrm{SST} - T_{10})}}{dx} \right] \quad (3)$$

$$\frac{dQ_L}{dx} = \rho L_w C_Q \left[\overline{(q_s - q_{10})} \frac{d\bar{U}}{dx} + \bar{U} \frac{d\overline{(q_s - q_{10})}}{dx} \right], \quad (4)$$

where the overbar denotes the average value on the flight axis AB. The first terms on the right-hand side of (3) and (4) are the mechanical terms, while the second terms are the thermal and humidity terms, respectively. The respective contributions of the mechanical term and of the thermal/humidity term to the variation of Q_H and Q_L are presented in Figure 9b; these two contributions were similar for sensible heat flux and more variable for latent heat flux. During the low-pressure period the mechanical and thermal/humidity terms can act in the same or opposite sense, and the heat flux was completely dependent on the thermodynamic characteristics of the incoming air mass which had different origins in the three cases (see Table 2 and Figure 4). For November 1 and 2, where the variations of Q_H between cold and warm sectors were small (about 5 W m^{-2}; see Table 3), the bulk method gave small negative values (about -1 to -3 W m^{-2}), in agreement with the slight decrease of wind and the temperature difference given in Table 3 between the two sectors. This can be explained by the wind direction oriented toward the cold side. On these 2 days the decrease of Q_L, due to the mechanical term, was balanced by the increase of the humidity term. The latter was due to both the lower specific humidity of the air mass on the warm side with respect to the cold one (Figure 5) and the SST increase on the warm side which led to a higher surface specific humidity (assuming that the air at the surface was close to saturation) on the warm sector (see Table 3 and Figure 8). These two factors acted in the same way; that is, they increased the $(q_s - q_{10})$ term on the warm side. For October 31 the two terms acted in the same sense and corresponded to an airflow coming from the cold side. Some analogous remarks were reported during FASINEX by *Rogers* [1989].

During the high-pressure period, where the MABL flow came from the cold zone, the two terms acted in the same sense. The mechanical term, in general, was prevailing and resulted from an increase of the wind from the cold to the warm zone. The increase of the thermal/humidity term was linked to the advection of cold and dry air over the SST front.

In conclusion, the horizontal gradients of SST induced horizontal gradients of the surface turbulent heat fluxes, as reported during FASINEX, JASIN, and the experiment above the Gulf Stream. This inhomogeneity produced the baroclinic character of the MABL as observed during the Genesis of Atlantic Low Experiment (GALE) by *Wayland and Raman* [1989].

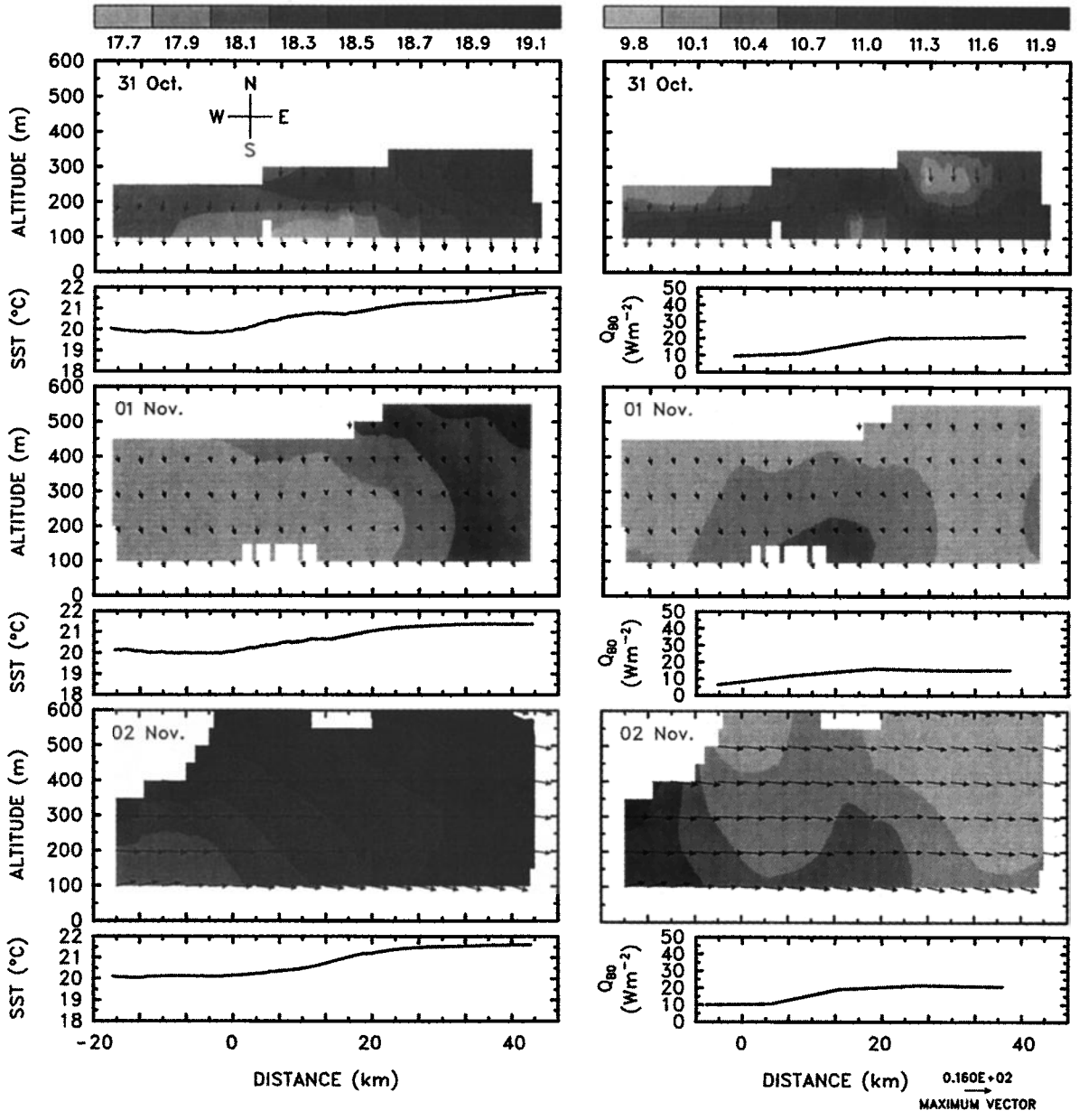

Figure 6a. (left) Potential temperature and (right) humidity mixing ratio in a vertical plane along the aircraft main axis. For (top) October 31 (middle) November 1, and (bottom) November 2. Arrows represent the horizontal wind. For each day the (left) sea surface temperature and (right) surface buoyancy flux along the same axis are also drawn. The horizontal distance on the reference axis is referred to the beginning of the SST increase in the cold zone.

6. Variation of the MABL Turbulent Characteristics Over the SST Front

The variation of the MABL turbulent characteristics over the SST front was analyzed, first case by case from the two-dimensional structure in the vertical plane described by the aircraft and second through a statistic on the profiles normalized with the appropriate local scales. The first approach was used to illustrate the large tendencies of the turbulent characteristics in the MABL. The statistical approach allows one to determine whether the parameterization based on the local scales was valid in the case of a MABL forced by a SST front. Analysis of the turbulence characteristics is presented for October 31 and November 11, where the airflow was parallel to the flight axis, and for November 2 and 13, where it was nearly perpendicular (see Figure 4). The statistical analysis includes the six cases.

6.1. Heat Fluxes

The fields of the sensible heat flux, latent heat flux, and buoyancy flux, given with the same unit to simplify the comparison, in the vertical plane parallel to SST gradient oriented from the cold to the warm sector, are presented in Figure 10a for October 31 and November 1 and in Figure 10b for November 2 and 13. Given that the fluxes were computed on non-overlapping, 25-km-long, straight and level runs, the initial field was composed of 30 to 40 values, which were interpolated and smoothed in order to obtain the large tendencies of the field. Figure 10a shows that the sensible heat, latent heat, and

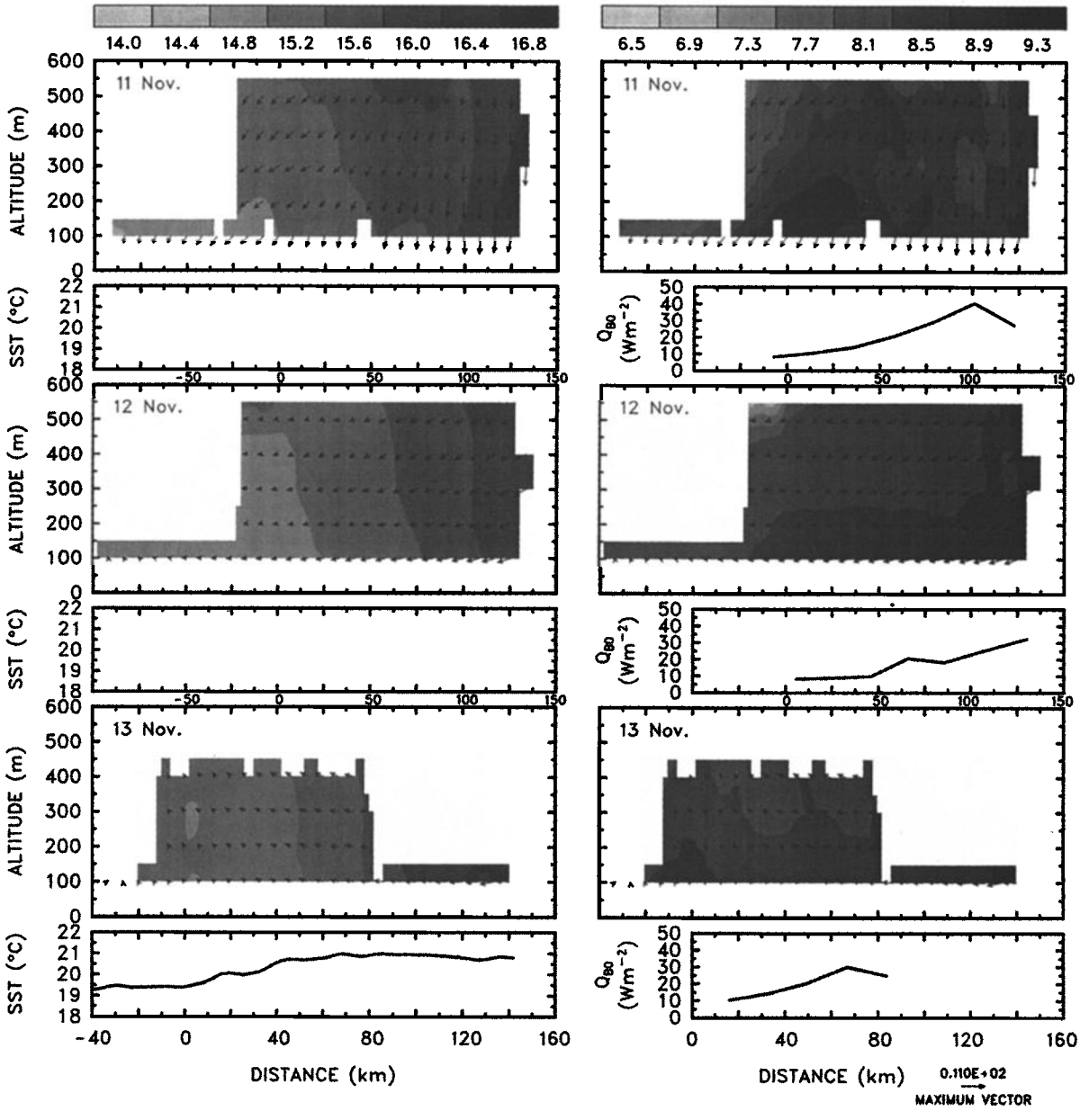

Figure 6b. Same as Figure 6a, but for November (top) 11, (middle) 12, and (bottom) 13.

buoyancy flux significantly increased from the cold to the warm part in the MABL when the wind coming from the cold sector was parallel to the flight axis (see Figure 4). The horizontal variations of heat fluxes on October 31 were mainly observed in the zone of SST gradient between the cold zone and the warm zone, whereas the values were more homogeneous on both extremities of the axis. On November 11 the increase of heat fluxes was also well related to the SST gradient. A decrease of the heat fluxes was observed at the extremity of the warm side on the homogeneous SST zone.

Figure 10b presents the variation of the heat fluxes above the SST front with the wind coming from the warm sector on November 12 and from the cold sector on the November 13 (see Figure 4). As for the preceding cases, the following remarks can be drawn: the increase of heat fluxes was encountered in the zone of SST increase.

From these observations one can conclude that the SST field controlled the vertical structure of the turbulent heat fluxes in the whole mixed layer. This effect was not related to the wind orientation and depended only on local conditions.

Figure 11 presents the profiles of sensible heat, latent heat, and buoyancy flux. The altitude was normalized by the local mixed layer thickness h, which was determined from the aircraft vertical soundings performed at the beginning, middle, and end of the main axis AB. As presented in section 4, the continuous variation of h along AB was thus deduced by interpolating between these three values. The flux profiles were computed each 25 km, and the local surface values, used for normalizing the flux, were deduced from extrapolation toward the surface of these individual profiles. Because we observe no change in the profile shape between the cold and warm sector, all the data are gathered together to obtain a normalized profile. The normalized profiles of the sensible heat, latent heat, and buoyancy fluxes were well fitted be-

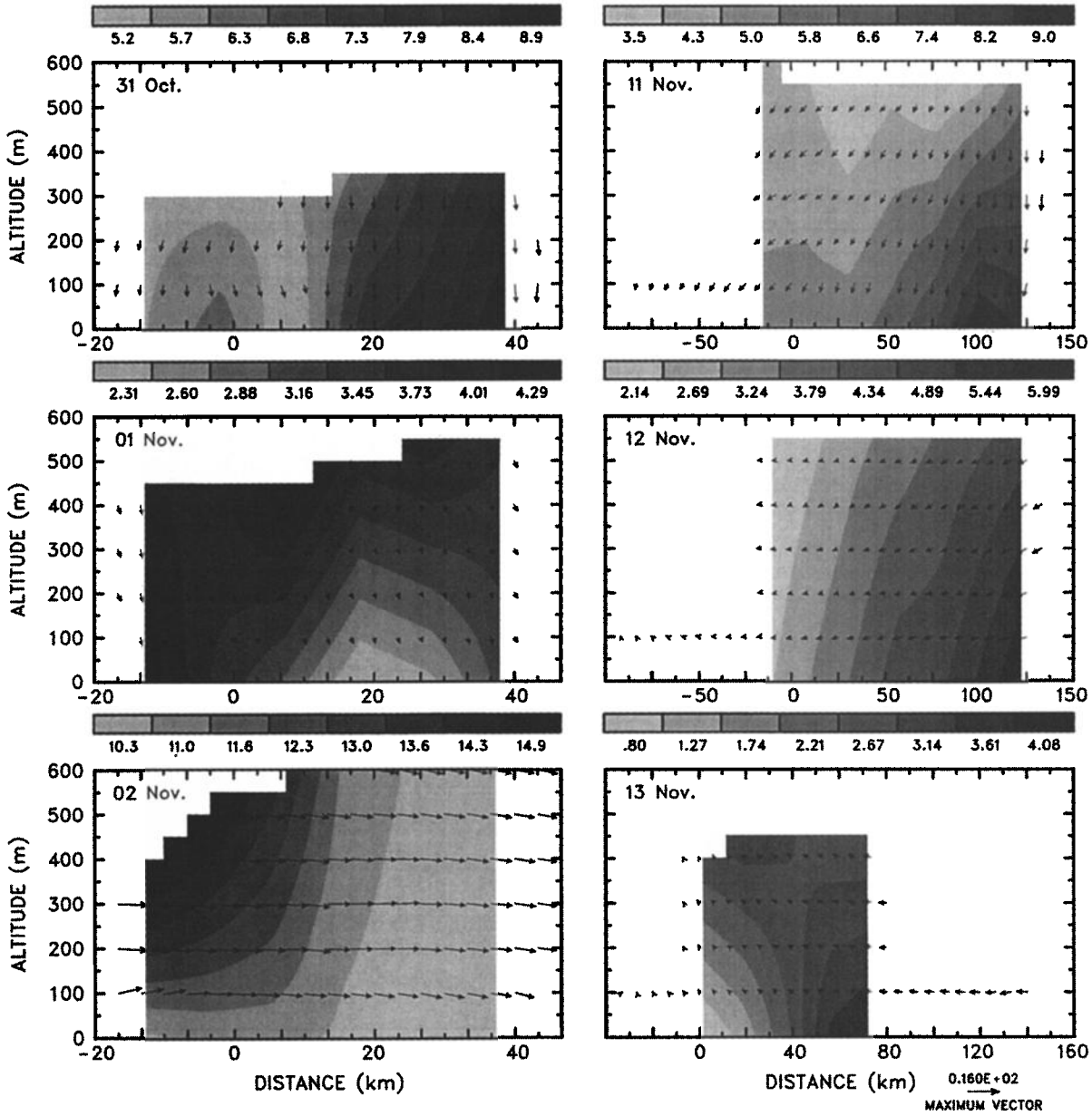

Figure 7. Horizontal wind vector (arrows) and wind velocity (colors) in the vertical plane along the aircraft main axis for (left) October 31 and November 2 and (right) November 11, 12, and 13.

tween $0.1h$ and h by the following expressions, represented by the solid curves in Figures 10a and 10b:

$$\frac{Q_H}{Q_{H0}} = 1 - 1.2\left(\frac{z}{h}\right), \tag{5}$$

$$\frac{Q_L}{Q_{L0}} = 1 - 0.8\left(\frac{z}{h}\right), \tag{6}$$

$$\frac{Q_B}{Q_{B0}} = 1 - 1.03\left(\frac{z}{h}\right), \tag{7}$$

where Q_B is the buoyancy flux. The three fluxes decrease linearly according to z/h and were in agreement with those derived from the Air Mass Transformation Experiment (AMTEX) and GALE data [*Chou and Ferguson*, 1991]. In particular, Q_B becomes zero at the top of the MABL. Concerning the entrainment at the MABL top, *Khalsa and Greenhut* [1989] show that the entrainment has a more important impact on the MABL over the warm sector than over the cold sector.

6.2. Velocity Variances

The velocity variances (Figures 12a and 12b) presented large variations in the MABL between the cold and warm sides, due to the wind variation and the local stability. The vertical velocity variance $\overline{w'^2}$ systematically increased from the cold to the warm side by a factor of 2 to 3, without relation to the incoming flow direction. The maximum value generally occurred in the lower third of the mixed layer. Its increase along the SST front was well correlated to the increase of the convective turbulence, in contrast with the variance of temperature $\overline{\theta'^2}$, which did not present any significant variation along the SST front.

The variance of the longitudinal $\overline{u'^2}$ and transversal $\overline{v'^2}$

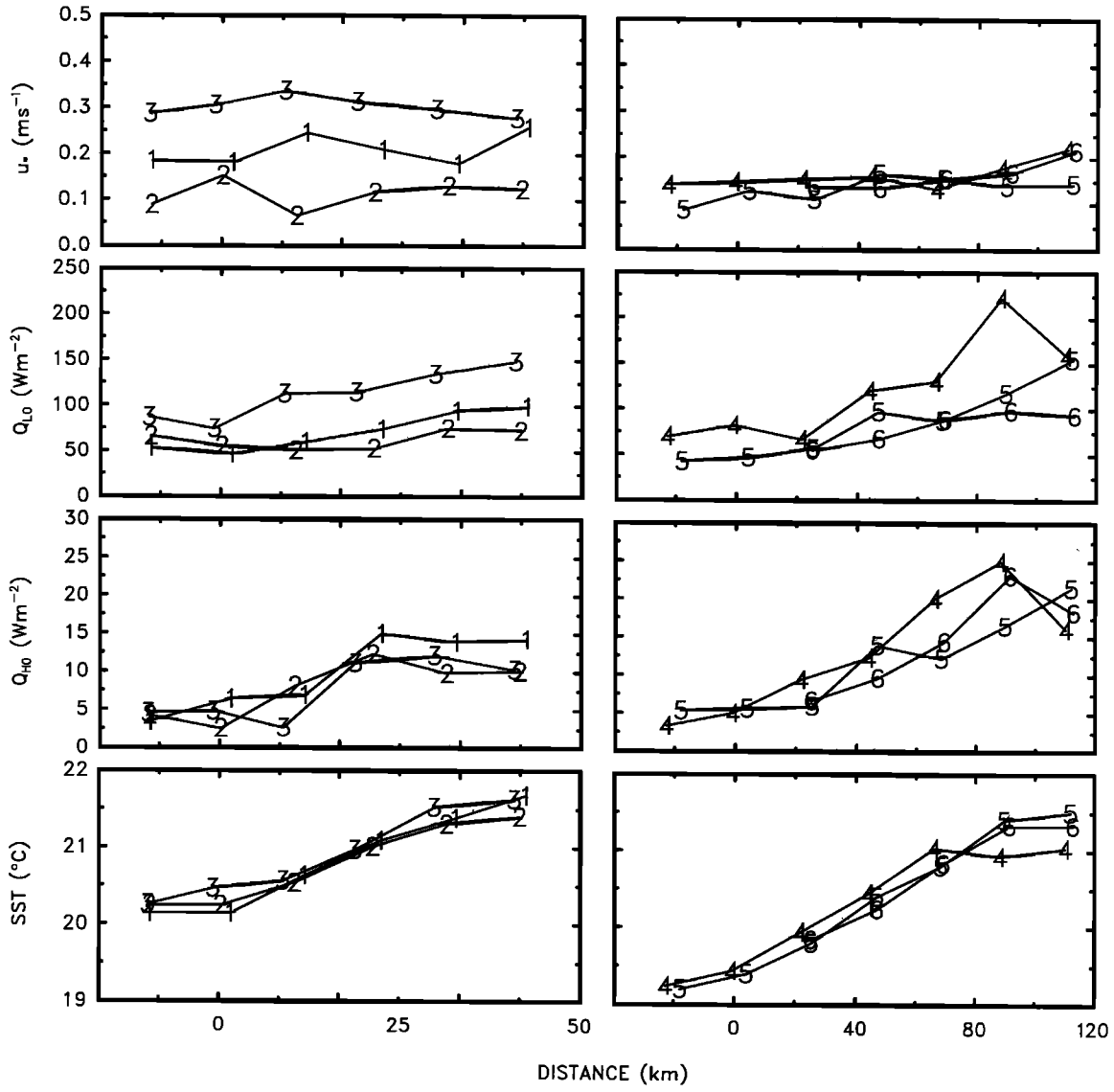

Figure 8. Variation of SST, surface sensible heat flux Q_{H0}, surface latent heat flux Q_{L0}, and friction velocity u_* along the aircraft track for (left) low-pressure and (right) high-pressure periods. The different days are represented by symbols (1–6) in Table 3.

wind components varied according to the wind. Their maximum value was located near the surface. Like $\overline{w'^2}$, they varied in the horizontal direction, but by a greater amount (3 to 5). During the high-pressure period the maximum was located on the warm side in conjunction with the increase of the wind from the cold to the warm sector. During the low-pressure period the wind was driven by the synoptic situation and no correlation with the SST front could be expected. For instance, on November 2 the variance maximum was located on the cold side. One can therefore conclude that the variances of the three wind components were related to the SST front during the high-pressure period, whereas only the vertical one presented such behavior during the low-pressure period where the influence of the synoptic situation drove the horizontal wind field.

7. Budget of Mean Parameters

7.1. Heat Budget

The heat budget was computed on November 11 and 12 in order to determine the principal mechanisms responsible for the increase (in depth and temperature) of the boundary layer from the cold to the warm sector. All the terms of the heat budget equation could not be computed from the measurements, which is why we used the ARPEGE model. As a first step, the terms that could be calculated from the data were compared with the results of the model. In a second step the model was used to compute all the terms of the budget.

Assuming that the vertical advection as well as the horizontal turbulent transfers can be neglected in the mixed layer, the mean potential temperature budget can be written as

$$\frac{\partial \bar{\theta}}{\partial t} + \bar{u}\frac{\partial \bar{\theta}}{\partial x} + \bar{v}\frac{\partial \bar{\theta}}{\partial y} + \frac{\partial \overline{w'\theta'}}{\partial z} + Q = 0, \qquad (8)$$

where $\bar{u}$ and $\bar{v}$ are the longitudinal and transversal wind components, respectively, in the aircraft coordinate system; the first term is the time evolution, the second term is the horizontal advection term, the third term is the vertical divergence of the heat flux, and the fourth term represents the radiation divergence and the water phase changes. Term 4 cannot be

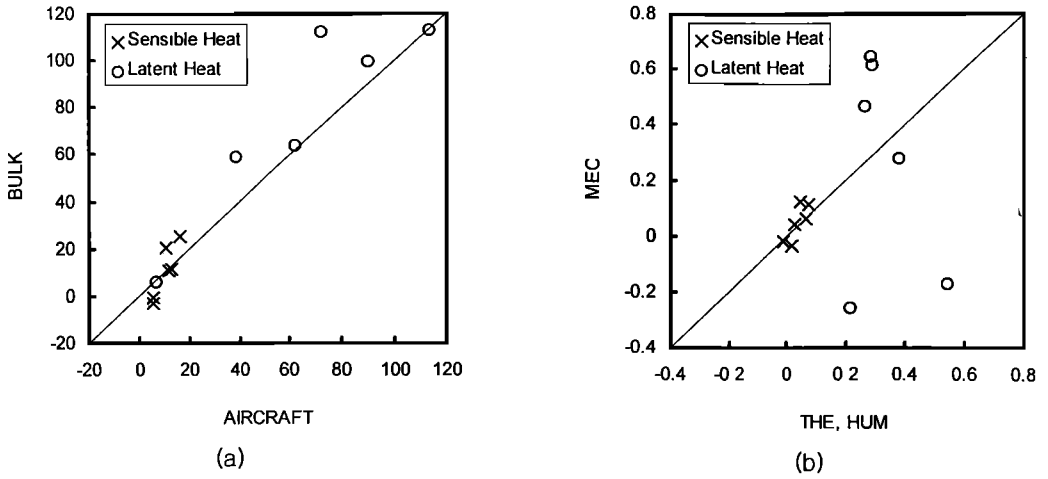

Figure 9. (a) Increase of the sensible heat flux (crosses) and latent flux (circles) from the cold to the warm side as measured by aircraft versus the same increase deduced from the bulk formulas. (b) Contribution of the thermal (THE) (crosses) and moisture (HUM) (circles) terms to the flux increase versus contribution of the mechanical term (MEC), as defined in equations (3) and (4).

neglected with respect to term 3 because the sensible heat flux is small (0 to 30 W m^{-2}). Integrating (8) from the sea surface up to the top of the mixed layer h, with $d\bar{\theta}/dt$ representing the sum of terms 1 and 2 in (8) and the entrainment flux parameterized with the entrainment coefficient C, we obtain

$$\left\langle \left(\frac{d\bar{\theta}}{dt} \right) \pm Q \right\rangle = \frac{(1 + C)(\overline{w'\theta'})_0}{h}. \quad (9)$$

7.1.1. Sensible heat flux divergence estimation. From the values of h and the surface flux Q_{H0} given in Table 3 and with C estimated as 0.2 from the sensible heat flux profile expressed by (5), the term on the right-hand side of (9) was computed in the cold and warm sides of the SST front (Table 4). It was systematically smaller in the cold zone (mean value of 0.05°C h^{-1}) than in the warm zone (mean value of 0.15°C h^{-1}) during the anticyclonic period and on October 31. On November 1 and 2, its variation was weak.

7.1.2. Advection term estimation. We estimated some components of the term $d\bar{\theta}/dt$ from aircraft and ship data and from the ARPEGE model. The advection term (2) of (8) was estimated from aircraft measurements. On November 11 and 12, only the advection along the flight axis could be calculated. The method used to calculate the thermal horizontal gradient was analogous to that developed by *Lenschow et al.* [1980], who estimated the accuracy between 50 and 100% of the calculated values. We computed the z integral of term 2 of (8) between the lowest and the highest flight level. We compared the longitudinal advection (term 2 of (8)) (denoted 3a on Figure 13) and the sensible heat flux divergence (term 3 of (8)) (denoted 1a on Figure 13) measured along the flight with those obtained from the ARPEGE model (symbols 1 and 2, respectively, in Figure 9) for the anticyclonic cases of November 11 and 12. The values ranged between −0.4 and +0.2°C h^{-1} (Figures 13a and 13b). The large tendency as well as the order of magnitude are well reproduced by the model along the flight axis, although some local differences appeared between experiment and model. The values of the longitudinal advection were close to zero in the cold area and negative in the warm area, reaching −0.3 and −0.15°C h^{-1} for November 11 and 12, respectively. The advection therefore acted, in a sense, to cool the MABL in the warm side. On the contrary, the heat flux divergence increased from the cold to the warm side, with a heating rate reaching 0.1 to 0.2°C h^{-1}. Figure 13 presents, for November 11 and 12, the various terms of the heat budget (advection and turbulent transport) deduced from the ARPEGE model. For the 2 days, these two terms were quite balanced in the cold side but not in the warm side, where they resulted in a cooling between −0.1° and −0.2°C h^{-1}. The two other terms of the budget (time variation and radiative divergence) and also the contribution of the term errors must explain this unbalance in the warm side.

7.1.3. Time variation estimation. From ship measurements (whose location is indicated in Figures 3 and 13) the time evolution (term 1 of (9)) was computed on a period of 5 hours including the flights. We found a quasi-stationary situation for November 11, where the ship was located in the warm side, and a considerable cooling (−0.19°C h^{-1}) for November 12, where the ship was located in the middle of AB. This term therefore could not explain the heat loss computed from the other terms at the ship location on November 11. On November 12 it also did not agree with the other terms that vanished at the ship location. The heat budget must therefore be balanced by a radiation divergence term, which could become

Table 4. Evolution of the Term on the Right-Hand Side of (9) for Each Day in the Cold and Warm Sector

Date	Position	Term
Oct. 31	A	0.054
	B	0.11
Nov. 1	A	0.044
	B	0.061
Nov. 2	A	0.054
	B	0.080
Nov. 11	A	0.049
	B	0.13
Nov. 12	A	0.032
	B	0.11
Nov. 13	A	0.042
	B	0.30

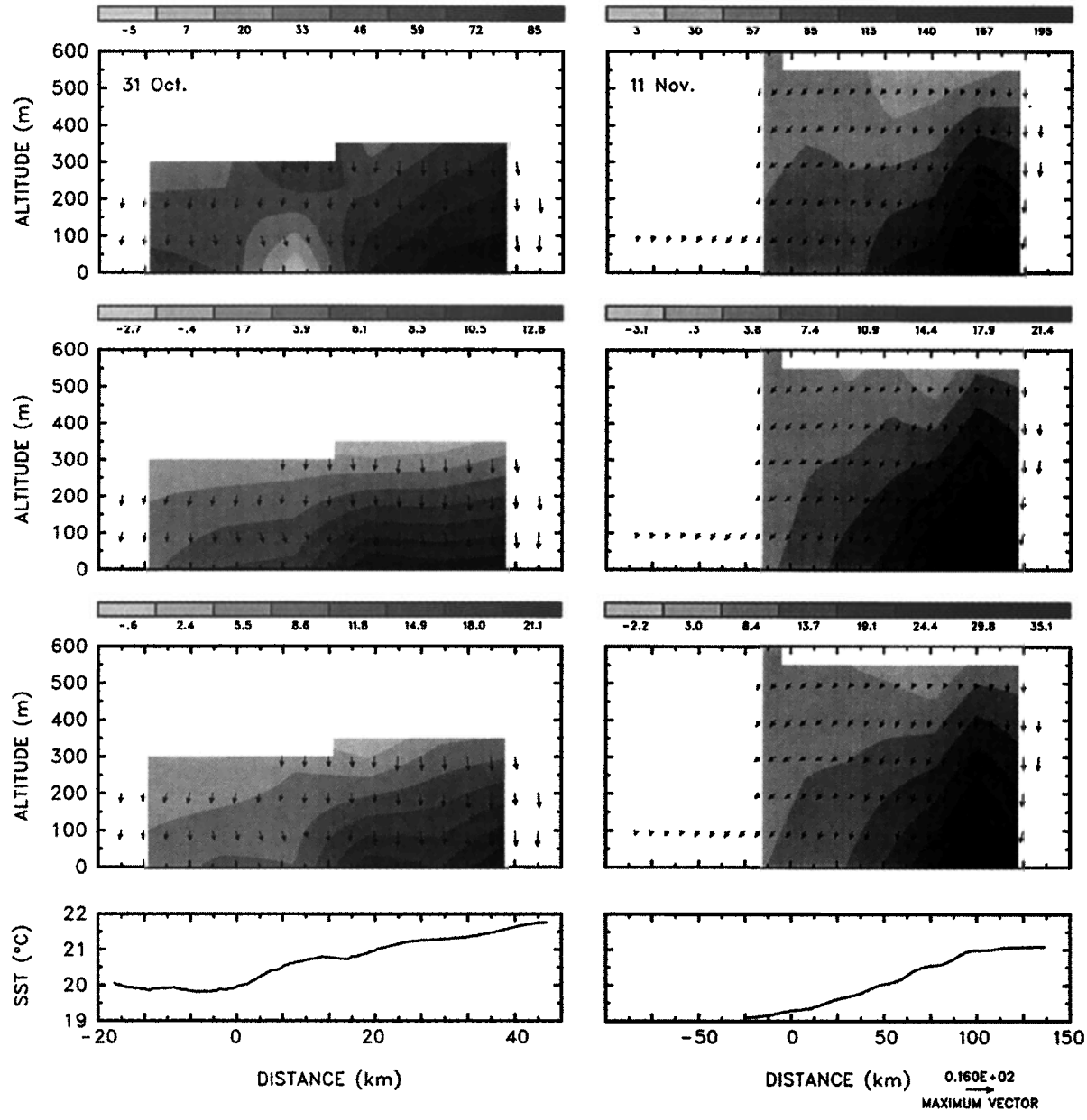

Figure 10a. (top) Latent heat flux, (middle) sensible heat flux, and (bottom) buoyancy flux in a vertical plane along the aircraft main axis as well as SST for (left) October 31 and (right) November 11. On these days the flow is approximately parallel to the flight axis.

large when clouds are present in the boundary layer. In this case, cloud-radiation interactions produce a temperature increase in the MABL. The heat budget of Figure 13 could be balanced with a heat supply of 0.1° to 0.2°C h^{-1}. This amount is similar to the values found by *Roach and Slingo* [1979] during JASIN with a longwave radiation transfer model.

To summarize, the heat budget was closely balanced in the cold side of the SST front between the advection and sensible heat flux divergence, whereas in the warm side these two terms resulted in a heat loss which required the taking into account of the influence of radiation divergence.

7.2. Momentum Budget

Our purpose was to analyze how the ageostrophic wind components induced by the horizontal temperature gradient in the MABL could balance the divergence of the momentum flux. We first computed the profile of the geostrophic wind in the MABL from the horizontal gradient of temperature, and, second, we adopted a linear variation of the wind profile in the MABL, which allowed us to compute the ageostrophic terms from the momentum budget equation. From the temperature horizontal gradients, measured along and across the flight axis, we can estimate the geostrophic wind shear, in the aircraft-related coordinate system, from the relations

$$\frac{\partial u_g}{\partial z} = -\frac{g}{fT}\frac{\partial T}{\partial y} = A_{gu}, \tag{10}$$

$$\frac{\partial v_g}{\partial z} = \frac{g}{fT}\frac{\partial T}{\partial x} = A_{gv}, \tag{11}$$

where $f = 2\Omega \sin \phi$, $\Omega = 7.292 \times 10^{-5}$, ϕ is latitude, g (= 9.8 m s^{-2}) is gravity, and T is the mean air temperature. We

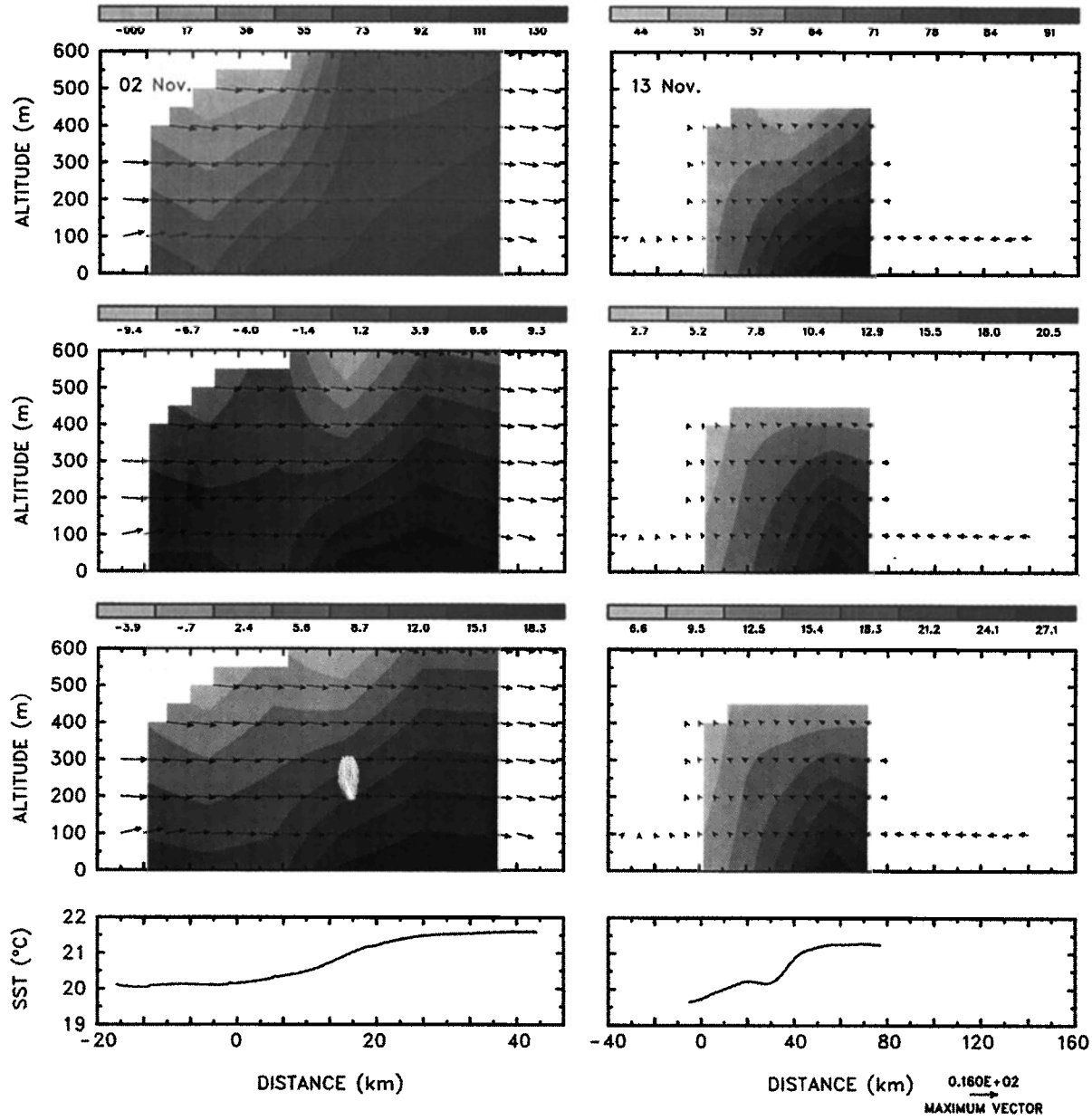

Figure 10b. Same as Figure 10a, but for November (left) 2 and (right) 13, where the flow is approximately perpendicular to the flight axis.

computed these values on October 31 and November 11, where the flight axis was almost parallel to the mean wind. On October 31 the flight plane allowed the determination of the two components of the geostrophic wind shear, whereas on November 11, only the longitudinal component could be computed. The perpendicular component was determined from the ARPEGE model. On October 31 the mean values computed along the longitudinal and transversal flight axis were 0.001 and 0.004 s^{-1}, respectively (see Table 5). Since $\partial u_g/\partial z$ and $\partial v_g/\partial z$ were positive (the longitudinal temperature gradient was positive, and the transversal one negative), u_g and v_g increased from the sea surface up to the top of the boundary layer. The profiles of the geostrophic components can be deduced from the z integral of (13) and (14), assuming as boundary conditions that $u_r = u_g$ and $v_r = v_g$ at the top of the mixed layer. The mean momentum budget equation can be written as

$$\frac{du_r}{dt} - f(v_r - v_g) = -\frac{\partial \overline{u'w'}}{\partial z} \tag{12}$$

$$\frac{dv_r}{dt} + f(u_r - u_g) = -\frac{\partial \overline{v'w'}}{\partial z} \tag{13}$$

where the index "r" is related to the real wind and the index "g" is related to the geostrophic wind. These equations can be simplified in the following form if we assume that $v_r = 0$ and the wind varies little with time:

$$u_r \frac{\partial u_r}{\partial x} + f(v_g) = -\frac{\partial \overline{u'w'}}{\partial z} \tag{14}$$

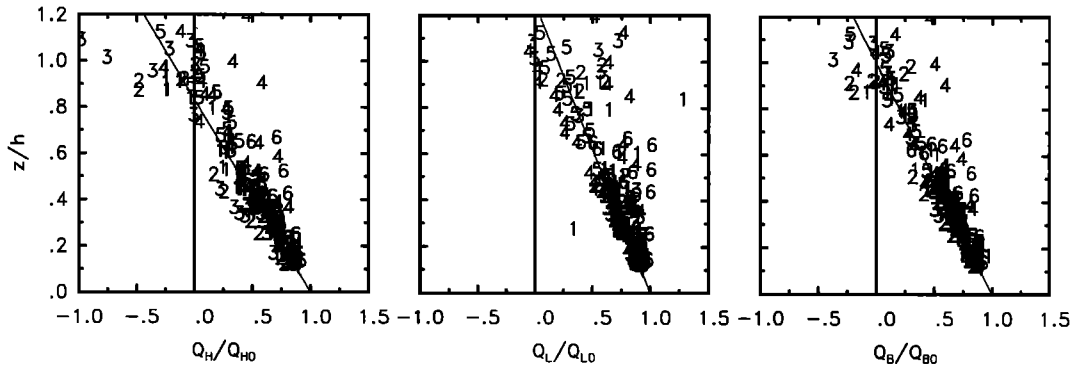

Figure 11. (left) Sensible heat, (middle) latent heat, and (right) buoyancy flux profiles. The fluxes are normalized by their surface value, and the altitude is normalized by the mixed layer thickness. The symbols refer to the various days (see Table 3).

$$f(u_r - u_g) = -\frac{\partial \overline{v'w'}}{\partial z} \tag{15}$$

In these relations, the momentum turbulent fluxes are calculated along the mean wind axis. If we further assume that the profiles of the wind and the geostrophic components are linear as well as some other hypotheses explained in the appendix, integrating (14) and (15), with respect to the altitude, from z to the top of the MABL h, leads to the following expressions:

$$\overline{u'w'}(z) = -f\frac{h^2}{2}HA_{ru}\left[\left(\frac{A_{gv}}{HA_{ru}} + \frac{A_{ru}}{f}\right)\left(1 - \frac{z}{h}\right)^2 - 2\frac{u_{rh}}{fh}\left(1 - \frac{z}{h}\right)\right], \tag{16}$$

$$\overline{v'w'}(z) = f\frac{h^2}{2}(A_{gu} - A_{ru})\left(1 - \frac{z}{h}\right)^2 \tag{17}$$

with $H = \partial h/\partial x$ assumed to be constant. If the advection terms are neglected, (16) and (17) then become

$$\overline{u'w'}(z) = -f\frac{h^2}{2}(A_{gv} - A_{rv})\left(1 - \frac{z}{h}\right)^2 \tag{18}$$

$$\overline{v'w'}(z) = f\frac{h^2}{2}(A_{gu} - A_{ru})\left(1 - \frac{z}{h}\right)^2 \tag{19}$$

On October 31 and November 11 the scatter of the stress profiles measured along the flight axis did not allow accurate determination of local value of the momentum flux divergence. We reduced the scatter of the data by compositing all the profiles measured along the flight axis. We thus used a nondimensional form of the momentum budget with the local values of the characteristic scales u_* and h. The normalized momentum fluxes computed for October 31 and November 11 above the SST front were averaged in nonoverlapping bins of $0.2z/h$. The resulting stress profiles, $\overline{u'w'}/u_*^2$ and $\overline{v'w'}/u_*^2$ as well as the standard deviation within each bin are presented in Figure 14a and 14b. The profile of $\overline{u'w'}/u_*^2$ decreased from very low values at h to -1 at the surface, while that of $\overline{v'w'}/u_*^2$ was close to zero through the whole MABL.

Also plotted in Figures 14a and 14b is the normalized mean stress deduced from (18) and (19), without and with taking into account the advection term (solid and dashed curves, respectively). The good agreement between the observed and modeled stress profiles (especially when taking the advection into account) shows that our estimations of geostrophic and ageostrophic terms were correct. This analysis of momentum budget therefore demonstrates that the real wind in the MABL strongly departed from the geostrophic wind and that this departure appeared to be driven by the mean flow associated with the surface thermal forcing due to the SST front. The decrease of the wind with altitude in the MABL suggests the existence of an inversed flow at higher altitude corresponding to a thermally induced circulation across the SST front. This kind of circulation cannot be analyzed with aircraft measurements alone. Several experimental works such as those of *Businger and Shaw* [1984] during JASIN, *Sweet et al.* [1981] over the Gulf Stream, *Hsu* [1984], and *Khalsa and Greenhut* [1989] reported the presence of a secondary circulation associated with an SST front. *Giordani et al.* [this issue] showed from the ARPEGE analysis that the surface heat flux was an important local source of ageostrophy. In particular, they found a good correlation between the increase of the ageostrophic circulation and the increase of the sensible heat flux. From the ARPEGE model, *Giordani et al.* [this issue] concluded that a simplified model such as that presented by *Hsu* [1984] allows one to identify only one source of the secondary circulation in the baroclinic MABL in SEMAPHORE. Identifying all the forcings, giving rise to the secondary circulation requires the analysis of the budget equation of the ageostrophic wind.

8. Conclusions

We present in this paper the structure of the marine atmospheric boundary layer (MABL) over the SST front, studied mainly with two aircraft and a ship in different meteorological conditions. Three cases of low pressure, where the MABL structure was rather affected by synoptic effects, and three

Table 5. Estimation of the Vertical Gradient of the Geostrophic Wind in the MABL

	Oct. 31		Nov. 11	
	A	B	A	B
$\partial v_g/\partial z$, s^{-1}	5×10^{-3}	3×10^{-3}	5×10^{-4}	5×10^{-3}
$\partial u_g/\partial z$, s^{-1}	3×10^{-4}	1×10^{-3}	5×10^{-4}	6×10^{-4}

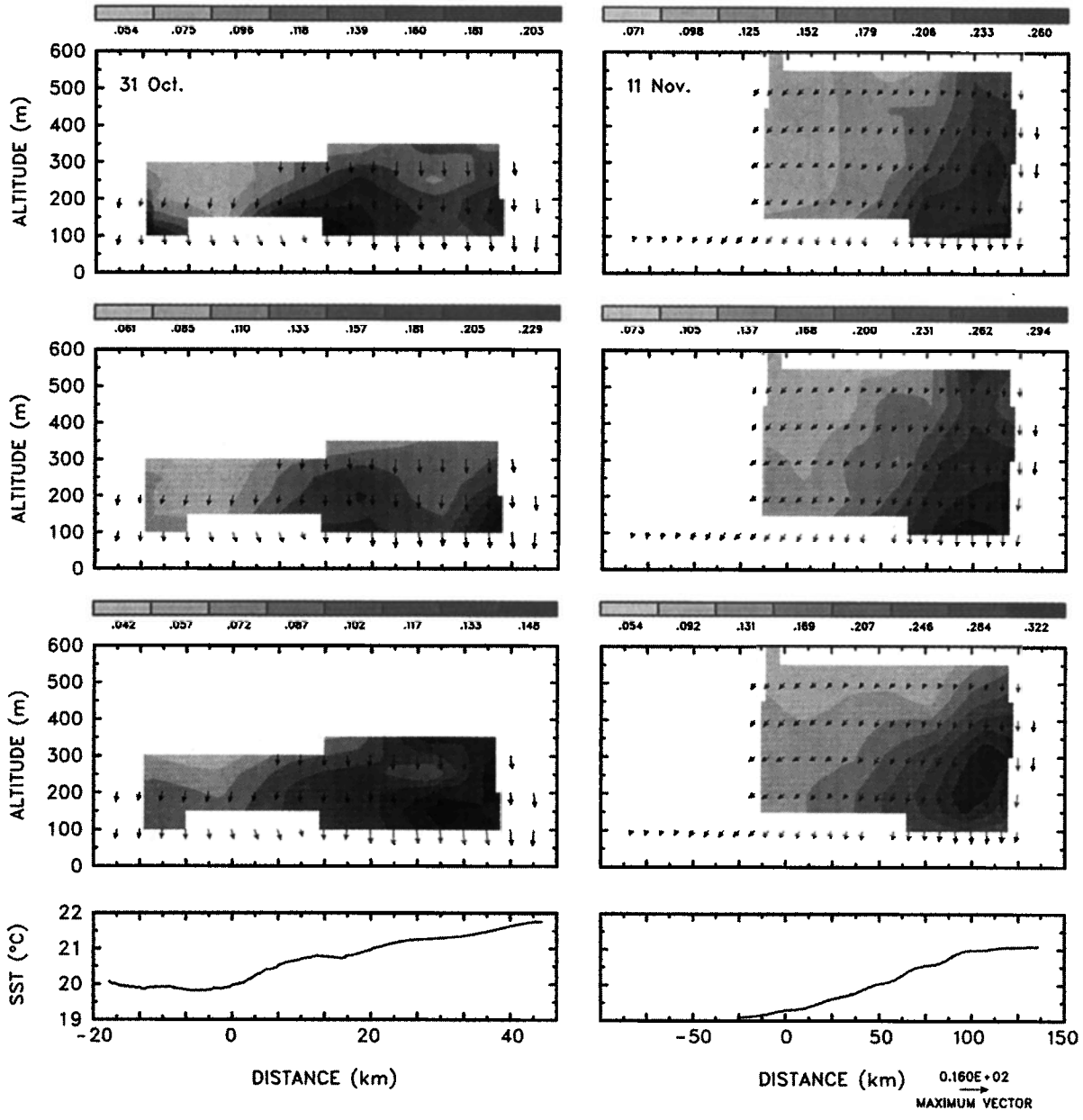

Figure 12a. Same as Figure 10a, but for the variances of wind components in $m^2\ s^{-2}$, (top) longitudinal component u'^2, (middle) transversal component v'^2, and (bottom) vertical component w'^2.

cases of high pressure, with predominant local effects, were presented. For each case, the influence of the incoming air direction with respect to the oceanic front orientation was taken into account.

For the six cases, the AVHRR pictures did not show any relation between the SST field and the cloud cover. The MABL was systematically thicker on the warm side than on the cold side by 100 to 300 m in conjunction with the heat budget of the MABL. Despite the low values of the SST gradients encountered during SEAPHORE (about 1° to 2°C/100 km), with respect to those encountered in the other experiments such as JASIN and FASINEX, the mean MABL structure, described from aircraft data collected in a vertical plane crossing the oceanic front, presented large variations that were characterized by (1) an atmospheric horizontal gradient of about 1°C per 100 km, in the whole depth of the mixed layer; (2) an increase of the wind intensity (by a factor of 2) from the cold to the warm side, during anticyclonic periods when the synoptic wind blew from the cold side; (3) a decrease of the wind with height, especially on the warm side; (4) a systematic increase of the surface sensible heat (latent heat) flux from the cold to the warm side due to the increase of the wind and of the temperature (specific humidity) difference between the surface and the air; (5) a large variation of the stability parameter from 1 day to another, but a small variation from the cold to the warm sector; (6) an increase of the turbulence parameters from the cold to the warm side, in conjunction with the MABL thickening, but an identical shape of the normalized profiles, whatever the horizontal position over the SST front may be; the second-order terms were slightly affected by the horizontal temperature gradient.

The mean heat and momentum budgets were highly influ-

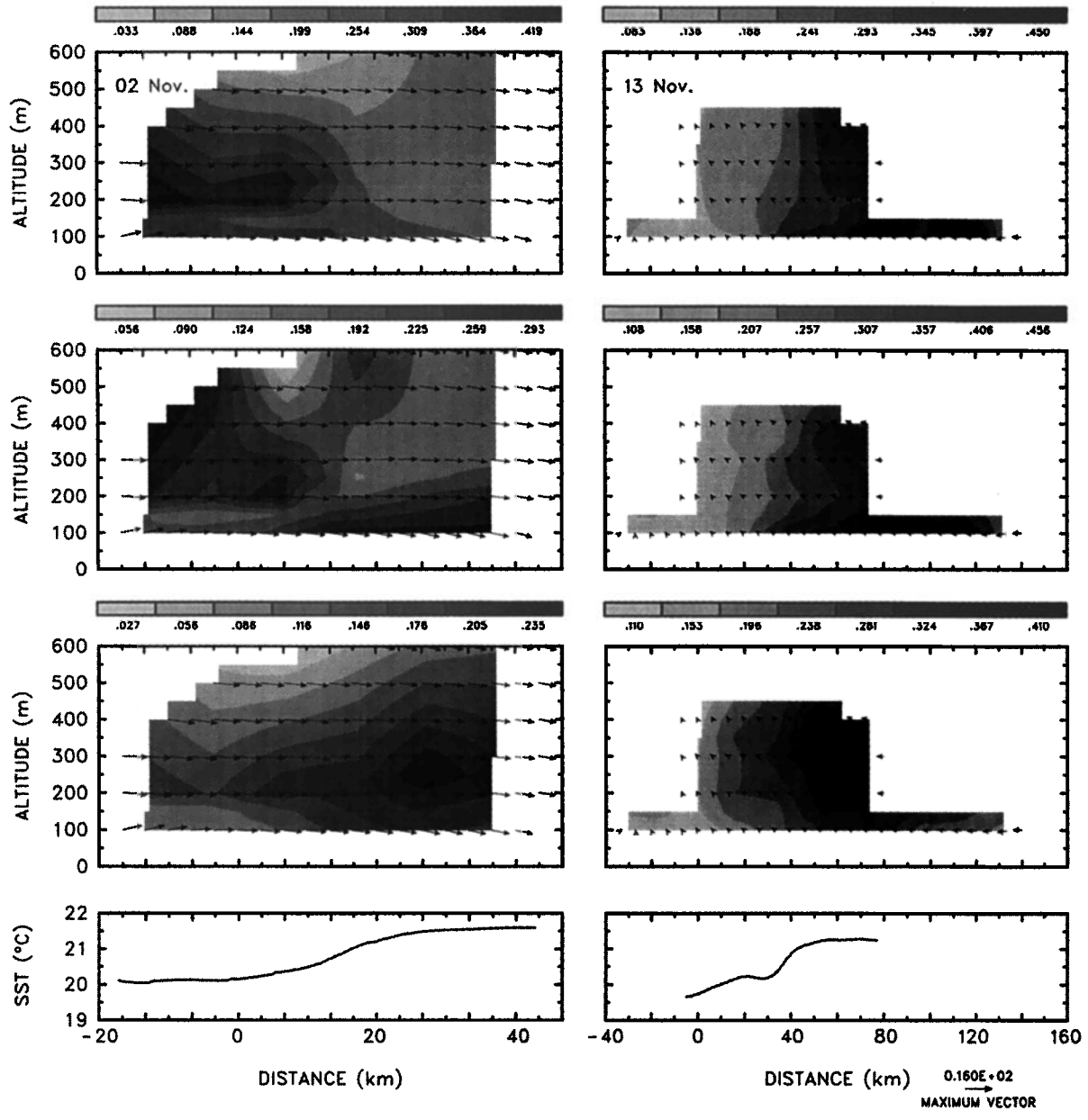

Figure 12b. Same as Figure 12a, but for November (left) 2 and (right) 13, where the flow is perpendicular to the flight axis.

enced by the horizontal temperature gradient. The mean heat budget was considerably different between the cold and warm sides. The experimental data and the results of the simulation gave the same tendency from the cold to the warm side; if the budget is nearly balanced between advection and turbulent flux divergence on the cold side, it was not the case on the warm side, which required the supply of another term that was inferred to be the radiation divergence due to the clouds. From the momentum budget established with some hypotheses on the wind structure inside the MABL, the importance of the ageostrophic terms linked with the secondary circulation due to the SST front was demonstrated.

Appendix: Development of Momentum Equation in an Ageostrophic System

In those cases where the real wind blows from cold sector to warm sector, with a constant direction, the perpendicular component v_r may be small in the whole mixed layer. The magnitude of the wind, which is equivalent to the parallel component u_r, decreases with the altitude, most notably in the warm sector. Supposing that this decrease is linear, we can obtain two constant gradients

$$A_{ru} = \frac{\partial u_r}{\partial z}, \qquad A_{rv} = \frac{\partial v_r}{\partial z}.$$

An increase of two components in the geostrophic wind is given by

$$A_{gu} = \frac{\partial u_g}{\partial z}, \qquad A_{gv} = \frac{\partial v_g}{\partial z}.$$

If we suppose that two components in the real wind are equal to those in the geostrophic wind at the top of the mixed layer, the wind variation can be expressed by the following linear formulas:

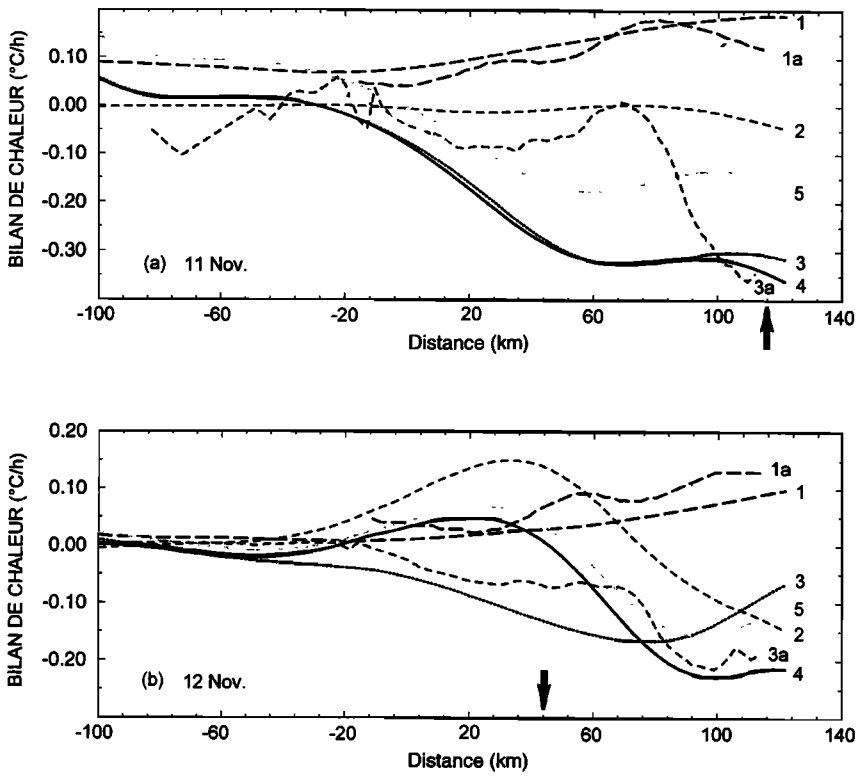

Figure 13. Evolution along the flight axis of different terms of the heat budget, deduced from ARPEGE, for November (a) 11 and (b) 12. Numbers are defined as follows: 1, heat flux divergence; 2, horizontal advection perpendicular to the flight axis; and 3, horizontal advection along the flight axis; 4, sum of terms 2 and 3; 5, sum of terms 1 and 4; 1a, heat flux divergence from aircraft measurements; and 3a, horizontal advection from aircraft measurements. Arrow indicate ship location.

$$u_r = A_{ru}(z - h) + u_{rh}, \quad \text{(A1)}$$

$$v_r = A_{rv}(z - h) + v_{rh}, \quad \text{(A2)}$$

$$u_g = A_{gu}(z - h) + u_{gh}, \quad \text{(A3)}$$

$$v_g = A_{gv}(z - h) + v_{gh}. \quad \text{(A4)}$$

A_{gu} and A_{gv} are determined by horizontal potential temperature gradient given by (13) and (14); A_{ru} and A_{rv} are determined by the least squares regression on horizontal wind data. Since $v_r = 0$, $A_{rv} = 0$. In the stationary case ($\partial u/\partial t = 0$ and $\partial v/\partial t = 0$), supposing that vertical component w_r is negligible in comparison with horizontal components, $v_{rh} = v_{gh} = 0$ and

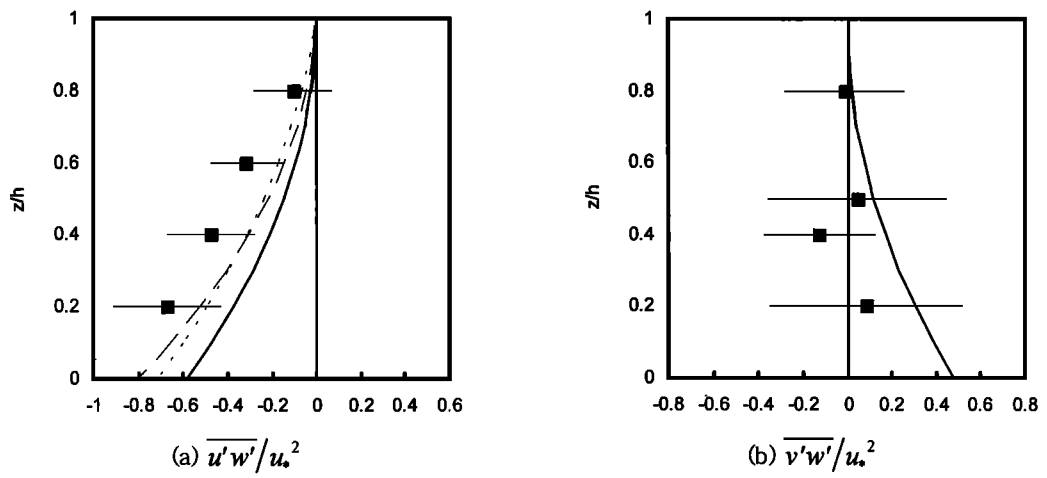

Figure 14. Profile of the normalized mean stress (a) along and (b) across the flight axis. Formulas (18) and (19) are represented by the dashed curve for October 31 and dotted curve for November 11; the solid curves represent the same terms for both days without advection. Squares represent the measured values averaged in nonoverlapping vertical bins. The measured values have been averaged in nonoverlapping vertical bins. The horizontal bars represent the standard deviations within each bin.

$u_{rh} = u_{gh}$ at the top of the MABL, we have the mean momentum budget as (17) and (18).

Integrating from z to h, (17) and (18) become:

$$\overline{u'w'}(z) = -f\frac{h^2}{2}A_{gv}\left(1-\frac{z}{h}\right)^2 + \frac{h^3}{6}\frac{\partial A_{ru}^2}{\partial x}\left(1-\frac{z}{h}\right)^3 - \frac{h^2}{2}\left(u_{rh}\frac{\partial A_{ru}}{\partial x} - A_{ru}^2 H\right)\left(1-\frac{z}{h}\right)^2 - A_{ru}u_{rh}hH\left(1-\frac{z}{h}\right) \quad \text{(A5)}$$

$$\overline{v'w'}(z) = f\frac{h^2}{2}(A_{gu}-A_{ru})\left(1-\frac{z}{h}\right)^2 \quad \text{(A6)}$$

where

$$\frac{\partial A_{ru}}{\partial x} = \frac{\partial}{\partial x}\left(\frac{\partial u_r}{\partial z}\right), \qquad H = \frac{\partial h}{\partial x}.$$

Considering that u_{rh}, the horizontal wind at h does not vary horizontally ($\partial u_{rh}/\partial x = 0$; see Plate 2); neglecting the second-order derivative and normalizing by u_*^2, we obtain finally

$$\frac{\overline{u'w'}(z)}{u_*^2} = -\frac{fh^2}{2u_*^2}HA_{ru}\left[\left(\frac{A_{gv}}{HA_{ru}}-\frac{A_{ru}}{f}\right)\left(1-\frac{z}{h}\right)^2 + 2\frac{u_{rh}}{fh}\left(1-\frac{z}{h}\right)\right], \quad \text{(A7)}$$

$$\frac{\overline{v'w'}(z)}{u_*^2} = f\frac{h^2}{2u_*^2}(A_{gu}-A_{ru})\left(1-\frac{z}{h}\right)^2. \quad \text{(A8)}$$

References

Arrit, R. W., Effects of large-scale flow on characteristic features of the sea breeze, *J. Appl. Meteorol.*, *32*, 116–125, 1993.

Brown, E. N., C. A. Friehe, and D. H. Lenschow, The use of pressure fluctuations on the nose of an aircraft for measuring air motion, *J. Clim. Appl. Meteorol.*, *22*, 171–180, 1983.

Businger, J. A., and W. J. Shaw, The response of the marine boundary layer to mesoscale variations in sea-surface temperature, *Dyn. Atmos. Oceans.*, *8*, 267–281, 1984.

Chou, S. H., and M. P. Ferguson, The western Gulf Stream during an intensive cold-air outbreak, *Boundary Layer Meteorol.*, *55*, 255–281, 1991.

Deardorff, J. W., Convective velocity and temperature scales for the unstable planetary boundary layer and for Rayleigh convection, *J. Atmos. Sci.*, *27*, 1211–1215, 1970.

Dupuis, H., P. K. Taylor, A. Weill, and K. B. Katsaros, Inertial dissipation method applied to derive turbulent fluxes over the ocean during the surface of the ocean, fluxes and interactions with the Atmosphere/Atlantic Stratocumulus Transition Experiment (SOFIA/ASTEX) and Structure des Echarges Mer-Atmosphere, Proprietes des Heterogeneites Oceaniques: Recherche Experimentale (SEMAPHORE) experiments with low to moderate wind speeds, *J. Geophys. Res.*, *102*, 21,115–21,129, 1997.

Durand, P., H. Dupuis, D. Lambert, B. Bénech, A. Druilhet, K. Katsaros, P. Taylor, and A. Weill, Comparison of sea surface flux measured by instrumented aircraft and ship during SOFIA and SEMAPHORE experiments, *J. Geophys. Res.*, this issue.

Eymard, L., et al., Study of the air-sea interactions at the mesoscale: The SEMAPHORE experiment, *Ann. Geophys.*, *14*, 986–1015, 1996.

Friehe, C. A., W. J. Shaw, D. P. Rogers, K. L. Davison, W. G. Large, S. A. Stage, G. H. Crescenti, S. J. S. Khalsa, G. K. Greenhut, and F. Li, Air-sea fluxes and surface layer turbulence around a sea surface temperature front, *J. Geophys. Res.*, *96*, 8593–8609, 1991.

Giordani, H., S. Planton, B. Bénech, and B.-H. Kwon, Atmospheric boundary layer response to sea surface temperatures during the SEMAPHORE experiment, *J. Geophys. Res.*, this issue.

Guymer, T. H., J. A. Businger, K. B. Katsaros, W. J. Shaw, P. K. Taylor, W. G. Large, and R. E. Payne, Transfer processes at the air-sea interface, *Philos. Trans. R. Soc. London, Ser. A*, *308*, 253–273, 1983.

Hsu, S. A., Sea-breeze-like winds across the north wall of the Gulf Stream: An analytical model, *J. Geophys. Res.*, *89*, 2025–2028, 1984.

Hsu, S. A., R. Fett, and P. E. La Violette, Variations in atmospheric mixed height across oceanic thermal fronts, *J. Geophys. Res.*, *90*, 3211–3224, 1985.

Khalsa, B. J. S., and G. K. Greenhut, Atmospheric turbulence structure in the vicinity of an oceanic front, *J. Geophys. Res.*, *94*, 4912–4922, 1989.

Lambert, D., Structure moyenne et turbulence de la couche limite atmosphérique au dessue de l'océan (Expérience SEMAPHORE), thèse de doctorat, 212 pp., Univ. Paul Sbatier, Toulouse, France, 1997. (Available from Cent. de Rech. Atmos., Lannemezan, France.)

Lambert, D., and P. Durand, Aircraft-to-aircraft intercomparison during SEMAPHORE, *J. Geophys. Res.*, this issue.

Lenschow, D. H., Aircraft measurements in the boundary layer, in *Probing the Atmospheric Boundary Layer*, edited by D. H. Lenschow, pp. 39–56, Am. Meteorol. Soc., Boston, Mass., 1986.

Lenschow, D. H., J. C. Wyngaard, and W. T. Pennel, Mean-field and second-moment budgets in a baroclinic, convective boundary-layer, *J. Atmos. Sci.*, *37*, 1313–1326, 1980.

Panofsky, H. A., and J. A. Dutton, *Atmospheric Turbulence, Model and Methods for Engineering Application*, 397 pp., Wiley Interscience, New York, 1984.

Physick, W., A numerical model of the sea-breeze phenomenon over a lake or gulf, *J. Atmos. Sci.*, *33*, 2107–2135, 1976.

Réchou, A., P. Durand, A. Druilhet, and B. Bénech, Turbulence structure of the boundary layer below marine clouds in the SOFIA experiment, *Ann. Geophys.*, *13*, 1075–1086, 1995.

Roach, W. T., and A. Slingo, A high resolution infrared radiative transfer scheme to study the interaction of radiation with cloud, *Q. J. Roy. Meteorol. Soc.*, *105*, 603–614, 1979.

Rogers, D. P., The marine boundary layer in the vicinity of an ocean front, *J. Atmos. Sci.*, *46*, 2044–2062, 1989.

Rogers, D. P., J. A. Businger, and H. Charnock, A numerical investigation of the JASIN atmospheric boundary layer, *Boundary Layer Meteorol.*, *32*, 373–399, 1985.

Sweet, W., R. Fett, J. Kerling, and P. E. La Violette, Air-sea interaction effects in the lower troposphere across the north wall of the Gulf stream, *Mon. Weather Rev.*, *109*, 1042–1052, 1981.

Wayland, R. J., and S. Raman, Mean and turbulent structure of a baroclinic marine boundary layer during the 28 January 1986 cold air outbreak (GALE 86), *Boundary Layer Meteorol.*, *8*, 227–254, 1989.

B. Bénech, A. Druilhet, P. Durand, and D. Lambert, Laboratoire d'Aérologie, Centre de Recherches Atmosphériques, UMR 5560, 65300 Lannemezan, France. (e-mail: benb@aero.obs.mip.fr).

H. Giordani and S. Planton, Centre National de Recherche Météorologique, URA CNRS 1357, Météo-France, Toulouse 31057, France. (e-mail: Giordani@meteo.fr;Serge.Planton@meteo.fr).

B.-H. Kwon, Department of Astronomy and Atmospheric Sciences, Kyungpook National University, Taegu 702-701, Korea. (e-mail: bhkwon@sirius.kyungpook.ac.kr).

(Received October 27, 1997; revised June 19, 1998; accepted July 1, 1998.)